X-RAY BACKSCATTER IMAGING FOR RADIOGRAPHY BY SELECTIVE DETECTION AND SNAPSHOT: EVOLUTION, DEVELOPMENT, AND OPTIMIZATION

By

DANIEL SHEDLOCK

A DISSERTATION PRESENTED TO THE GRADUATE SCHOOL
OF THE UNIVERSITY OF FLORIDA IN PARTIAL FULFILLMENT
OF THE REQUIREMENTS FOR THE DEGREE OF
DOCTOR OF PHILOSOPHY

UNIVERSITY OF FLORIDA

2007

For my daughter, Alyssa, and her future

ACKNOWLEDGMENTS

I would like to thank God, for the gifts he has given me that allow me to walk this path and complete this journey. I am truly thankful for all the gifts He has given me. I need to thank my family, Missy and my daughter, Alyssa, for their patience, support and sacrifices they have made. I also need to thank my most active advisors Dr. Edward Dugan and Dr. Alan Jacobs for the wisdom of their guidance, and encouragement along the way. They set the stage and environment for success. I need to thank Dan Ekdahl for his time and excellent work that have contributed to the success of many projects. Thank you, Warren Ussery for the financial funding to push the research far beyond the laboratory and prototyping stage. I am thankful for all my colleagues in the research group, the day-to-day interactions and constant exchange of ideas was invaluable. This work has been made possible by a collection of individuals who put forth a tremendous effort in laying the foundations years before I even walked onto the project. Thank you everyone who has helped contribute to my growth, learning and success each step of the way. To be successful and succeed, one has to be surrounded by great people, and I have worked with some of the very best. Financial acknowledgment:

- Lockheed Martin Space Systems Co.
- NASA, Langley Research Center
- NASA, Marshall Space Flight Center
- University of Florida, Department of Nuclear and Radiological Engineering

TABLE OF CONTENTS

LIST OF TABLES

LIST OF FIGURES

Abstract of Dissertation Presented to the Graduate School
of the University of Florida in Partial Fulfillment of the
Requirements for the Degree of Doctor of Philosophy

X-RAY BACKSCATTER IMAGING FOR
RADIOGRAPHY BY SELECTIVE DETECTION AND SNAPSHOT:
EVOLUTION, DEVELOPMENT, AND OPTIMIZATION

By

Daniel Shedlock

August 2007

Chair: Edward T. Dugan
Major: Nuclear Engineering Sciences

Compton backscatter imaging (CBI) is a single-sided imaging technique that uses the penetrating power of radiation and unique interaction properties of radiation with matter to image subsurface features. CBI has a variety of applications that include non-destructive interrogation, medical imaging, security and military applications. Radiography by selective detection (RSD), lateral migration radiography (LMR) and shadow aperture backscatter radiography (SABR) are different CBI techniques that are being optimized and developed.

Radiography by selective detection (RSD) is a pencil beam Compton backscatter imaging technique that falls between highly collimated and uncollimated techniques. Radiography by selective detection uses a combination of single- and multiple-scatter photons from a projected area below a collimation plane to generate an image. As a result, the image has a combination of first- and multiple-scatter components. RSD techniques offer greater subsurface resolution than uncollimated techniques, at speeds at least an order of magnitude faster than highly collimated techniques.

RSD scanning systems have evolved from a prototype into near market-ready scanning devices for use in a variety of single-sided imaging applications. The design has changed to

incorporate state-of-the-art detectors and electronics optimized for backscatter imaging with an emphasis on versatility, efficiency and speed. The RSD system has become more stable, about 4 times faster, and 60 % lighter while maintaining or improving image quality and contrast over the past 3 years.

A new snapshot backscatter radiography (SBR) CBI technique, shadow aperture backscatter radiography (SABR), has been developed from concept and proof-of-principle to a functional laboratory prototype. SABR radiography uses digital detection media and shaded aperture configurations to generate near-surface Compton backscatter images without scanning, similar to how transmission radiographs are taken.

Finally, a more inclusive theory of the factors affecting CBI contrast generation has tied together the past work of LMR with the more recent research in RSD. A variety of factors that induce changes in the backscatter photon field intensity (resulting in contrast changes in images) include: changes in the electron density field, attenuation changes along the entrance and exit paths, changes in the relative geometric positioning of the target, feature, illumination beam, and detectors. Understanding the interplay of how changes in each of these factors affects image contrast becomes essential to utilizing and optimizing RSD for different applications.

CHAPTER 1
INTRODUCTION

Background

Compton backscatter imaging (CBI) is a single-sided imaging technique in which the radiation source and the detection/imaging device are located on the same side of the object. As a result, CBI is a valuable non-destructive evaluation (NDE) tool because of its single-sided nature, penetrating abilities of radiation, and unique interaction properties of radiation with matter. Changes in the backscatter photon field intensity (resulting in contrast changes in images) are caused by differences in absorption and scattering cross sections along the path of the scattered photons. Since the inception of CBI, a diverse set of imaging techniques have evolved using both collimated and uncollimated detectors, coded apertures, and hard x-ray optics. Work here at the University of Florida focuses on backscatter Radiography by Selective Detection (RSD), Lateral Migration Radiography (LMR) and Shadow Aperture Backscatter Radiography (SABR).

Pencil Beam Compton Scatter X-ray Imaging

Pencil beam Compton scatter imaging uses a highly collimated pencil beam of radiation to interrogate objects. The pencil beams may vary in size from microns to centimeters, but usually consists of a near-parallel array of photons forming a tight beam.

Highly Collimated Techniques

As early as 1956, Odeblad and Norhagen[1] published results describing the effect of changes in electron density of a localized volume on Compton scattered photons. Changes in the electron density of the material were measured using a highly collimated detector and collimated ^{60}Co gamma source. The volume of material being interrogated is determined by the intersection of the field-of-view (FOV) of a collimated detector and the collimated source forming a small

voxel (Figure 1-1). Highly collimated configurations are dominated by first scatter components from the voxel because of the geometric configuration.

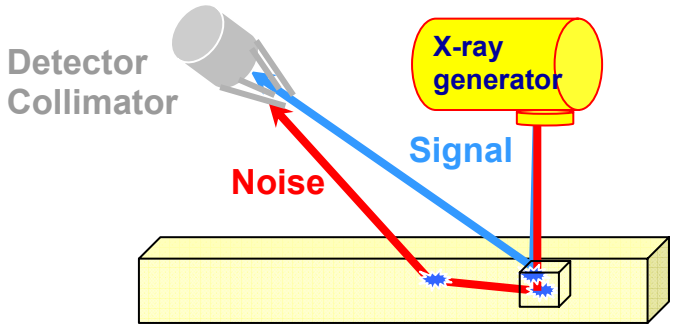

Figure 1-1. Highly collimated x-ray backscatter imaging, voxel by voxel

This first approach lends itself very well to x-ray backscatter tomographic imaging (TI).[2] Typically, a highly collimated source and set of concentric conical collimators[3] are used to isolate a volume in the object being interrogated; this volume is then represented as a voxel in the tomographic image. Multiple-scatter components are considered noise and removed with collimation. These TI backscatter devices then scan the object, voxel-by-voxel, to generate a three-dimensional image. Because the design of the collimators collects photons from a very small solid angle, the resulting signal at the detector is dominated by first-scatter components from the detector FOV. While highly collimated detectors and backscatter tomographic images provide some of the highest possible contrast images, some in three-dimensions, the acquisition time can be extremely long.

A technique called differential gamma scattering spectroscopy[4-5] uses the Compton shift in energy to determine the spatial location of the scattered beam. Although this technique is faster, it may require the use of high energy resolution detectors such as High Purity Germanium (HPGe) for some applications. Differential scattering spectroscopy has been revisited by

Lawrence Livermore National Lab (LLNL)[6] using room temperature detectors such as Cadmium Zinc Telluride (CZT) and a bremstraulung x-ray spectrum in a "new" technique called "virtual collimation". While dealing with a source spectrum complicates the spectral analysis, this is a variation of the gamma-ray techniques used to measure bubble size and distribution in two-phase flow.[7] Essentially a planar ^{241}Am source illuminated two-phase flow in a pipe. Compton shift in energy was used to determine the annular location and the size of the bubbles in the two-phase flow.

Dynamic radiography[8] is a type of scatter x-ray imaging (SXI) for interrogating objects in motion. The objects can have natural phonon motion, such as fluid flow, a beating heart, breathing lungs or phonon motion can be mechanically provided. This technique, like other highly collimated techniques, uses the intersection volume of a collimated radiation beam and detector. As the material in the illuminated volume oscillates, any significant changes in the cross sections will be measured in the detectors. The periodic motion provides a frequency correlation between the responses of different detectors, which would otherwise have independent responses, because a scattered photon detected in one detector can not be detected in the other detectors. Multiple detectors allow for the collection of data in different directions which can be used to generate three-dimensional images. This technique was used to measure the irregular motion in the beating heart of a dog caused by a decrease in the blood supply or by constriction or obstruction of the blood vessels.[9]

Uncollimated Backscatter Radiography

Because of the relatively long acquisition time required by highly collimated detectors, some CBI techniques use detectors without collimators. Instead of using the intersection of the detector FOV and illumination beam to form a voxel, the image is reconstructed from the assumption that all detected backscatter photons have originated from the illumination beam

spot.[10] A variety of commercial equipment is available for many scanning applications which include imaging trucks, cargo, people and luggage.[11] These techniques use very large detectors, sometimes on the order of square meters of detection area, to collect as many scattered photons as possible. While this uncollimated scanning approach is very fast and has a large number of applications, it is limited in subsurface resolution, because the signal is dominated by first-scatter, near surface components (Figure 1-2).

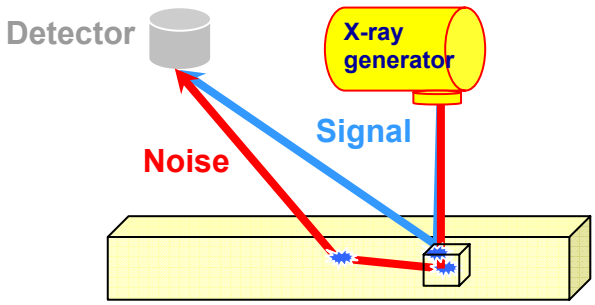

Figure 1-2. Uncollimated pencil beam CBI technique

Subsurface features that are located more than one mean-free-path (mfp) into the object can be difficult to image because the feature signal can be masked by near-surface, first-collision components. Collimation can be used to improve contrast and depth resolution, even for near surface features.

Radiography by Selective Detection

Radiography by selective detection (RSD) is a pencil beam Compton backscatter imaging technique that falls between highly collimated and uncollimated techniques. Uncollimated techniques are dominated by first-scatter components from near the surface of the interrogated object. While these techniques are very fast, uncollimated techniques lack subsurface resolution at depths beyond a mfp, and collimation often increases contrast and depth resolution even at shallow depths. Highly collimated techniques can image at depth, but are usually very slow

because the collimation typically only detects single-scatter components from a small voxel formed by an intersecting FOV between the illumination beam and the detector. Radiography by selective detection uses a combination of single- and multiple-scatter photons from a projected area below a collimation plane (CP) to generate an image (Figure 1-3). The collimation plane is a plane to which a photon must penetrate to enter the FOV of the detector.

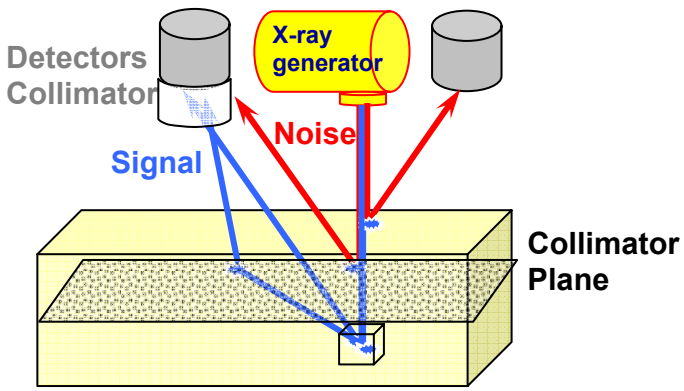

Figure 1-3. RSD collimated and uncollimated detector with collimation plane

Lateral Migration Radiography

A subset of RSD, Lateral Migration Radiography (LMR), was used for the detection of buried landmines.[12-20] The image contrast is dominated by third-order scatter x-ray components and higher. Because typically the illumination x-ray beam penetration barely extends to a depth much beyond the base of the mine, the mine (or surrounding soil) becomes a diverged scattered x-ray source for the properly collimated detectors (Figure 1-4). While second-order scatter components are still close to the penetrating beam, third and higher order scatter components migrate far enough from the original beam, to produce a laterally-spread scatter source in the landmine (or surrounding soil). Usually very large detectors (on the order of 0.3 m^2) are required to capture these laterally-spread, multiple-scatter components. The term LMR carried over to NDE experimentation,[21-23] but was later changed to RSD.

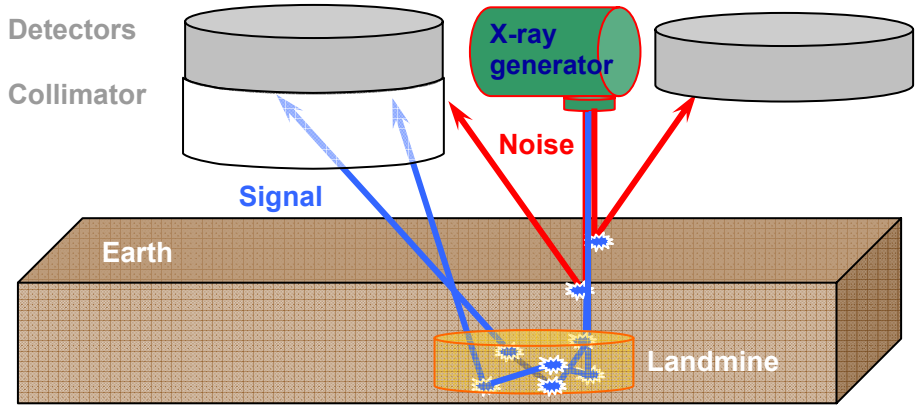

Figure 1-4. LMR collimated regime and uncollimated detector

RSD versus LMR

For RSD, a collimated source beam is used to illuminate an object of interest. Detector collimators are adjusted to preferentially receive signals from below a selected depth to remove scatter components which have not traversed the subsurface feature of interest and would, therefore, only add noise to the image. As with the landmine imaging, uncollimated detector information may be used to remove surface features. However, if the surface does not superimpose a strong signal on the subsurface, then it may not be necessary to perform such image processing.

RSD imaging for smaller features is different from LMR imaging for landmines. In many cases the illumination beam penetrates beyond the feature. As a result, the image contrast for the defects tends to be dominated by first- and/or second- scatter components, especially in low Z materials. These second-order scattered photons do not migrate very far from the path of first-scattered photons and the term RSD is used to described the process by which photons carrying information about the flaw are detected. This method differs from LMR, because the subsurface feature is relatively small compared to the mfp of the interrogation photons. As a result, multiple-scatter photons traverse the physical boundaries of the smaller feature and move

into the surrounding material. Smaller detectors also favor an RSD regime over an LMR regime, because the scattered photons can easily move outside the FOV of the smaller detectors. LMR is still an RSD technique because LMR selectively detects backscatter components that yield the greatest contrast enhancement.

Full-Field Illumination Compton Backscatter Imaging

Unlike pencil beam CBI techniques, full-field illumination techniques flood the entire FOV at once with x-rays. For these techniques, collecting and/or deciphering the backscatter field may become challenging. These techniques typically use a coded aperture or optic lenses for focusing.

Coded Aperture Imaging

When producing images it is often necessary to focus the photons onto some type of detection array. X-rays with less than 10 keV can be optically reflected, but beyond 10 keV the grazing angle for total external reflection becomes very small. At 30 keV the critical grazing angle for gold is 0.153 degrees.[24] In order to effectively image higher energy photons from multiple sources, coded aperture imaging uses straight-line optics, a coded mask such as shown in Figure 1-5, and a detection array capable of sensing straight-line projection patterns.[25] If only a single point source is present in the FOV, decoding the image based on straight-line optics is trivial. But when multiple source points, such as multiple stars, illuminate the FOV, multiple images are projected on the detector sensor array. These images can be decoded without distortion when the illuminating beams are parallel, which is the case for far-field objects like stars.

However, near field coded aperture imaging is more complicated; the source rays are not parallel because the scatter field does not come from far-field point sources. This results in artifacts or distortion of the images. One method to reduce the distortion is to obtain two images

with a mask and an anti-mask. When the mask and anti-mask images are summed, they constructively interfere; similarly, the difference of mask and anti-mask images cancel and leave noise.[26] Even with these advances, near-field coded aperture imaging does not yet have high resolution, and images may require very large acquisition times (on the order of hours) and very long deconvolution times (hours).[27]

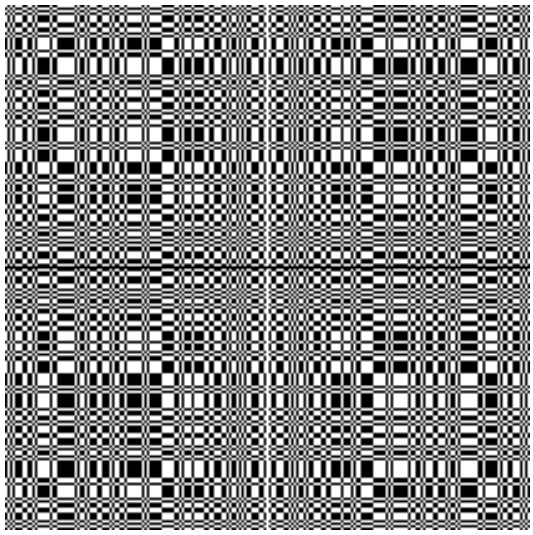

Figure 1-5. Example of a coded aperture using a Modified Uniformly Redundant Array (MURA)

Optical X-ray Focusing

Lobster eye optics is an optical x-ray imaging technique that has its birthplace in astronomy.[28] The idea of using the lobster eye to focus x-rays is conceptualized in Figure 1-6. Until recently, because of the very small critical grazing angle, devices for focusing hard x-rays (greater 10 keV) were very large and impractical.[24] But by using highly-polished, micro-tubular channels to focus the incoming x-rays a lobster eye imaging device can be constructed to focus x-rays. Physical Optics Corporation (POC) has proposed a hand-held lobster eye x-ray inspection device (LEXID) listed as an emerging technology. Figure 1-7 shows the design for the hand-held product without an x-ray source.

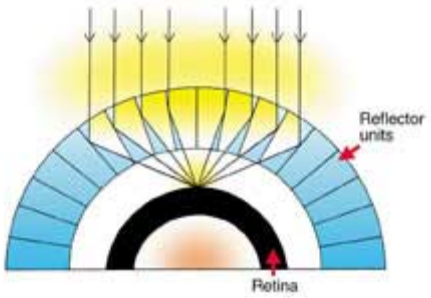

Figure 1-6. Conceptual drawing of lobster eye focusing parallel photons

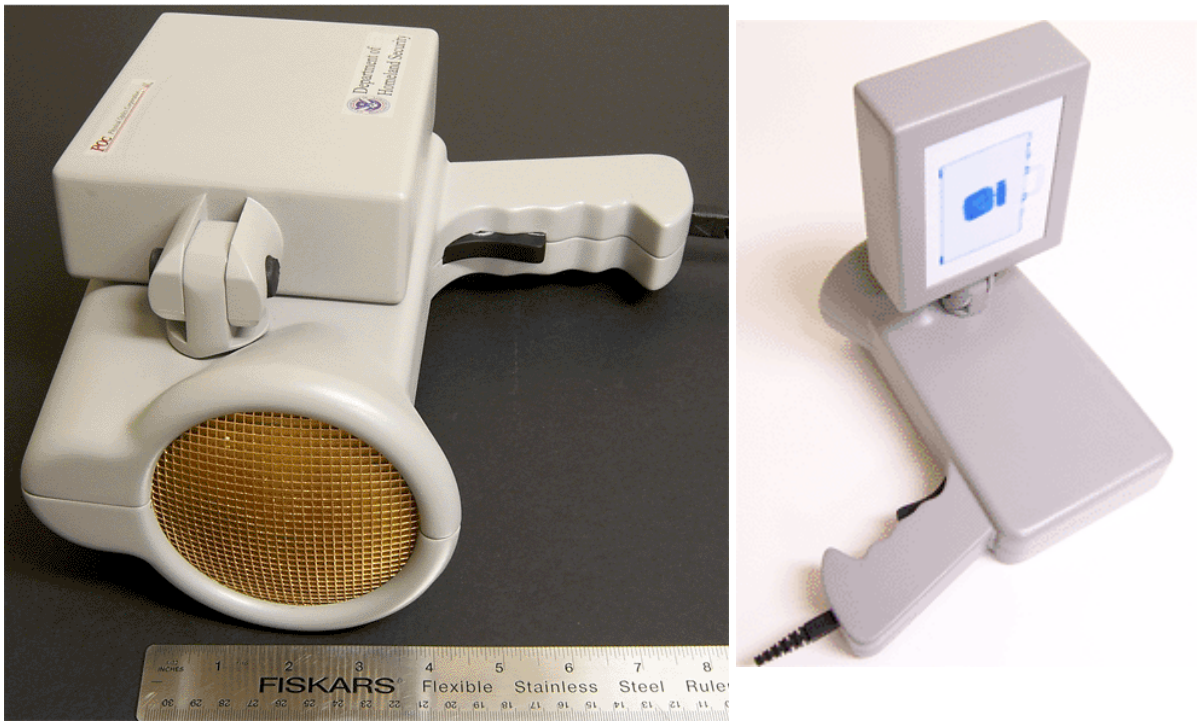

Figure 1-7. Emerging technology from POC for lobster eye hand held x-ray imaging device

CHAPTER 2
SCANNING SYSTEM OVERVIEW

Lockheed Martin Prototype System

In 2003 spray-on foam insulation (SOFI) from the external tank of the space shuttle tore loose during the Columbia launch and punctured the leading edge of the wing on the orbiter. Because the scatter x-ray imaging (SXI) research group at the University of Florida demonstrated the ability to detect simulated defects in the SOFI as part of a Lockheed Martin Space Systems Co. NDE initiative, funding was granted to build a prototype device (Figure 2-1).

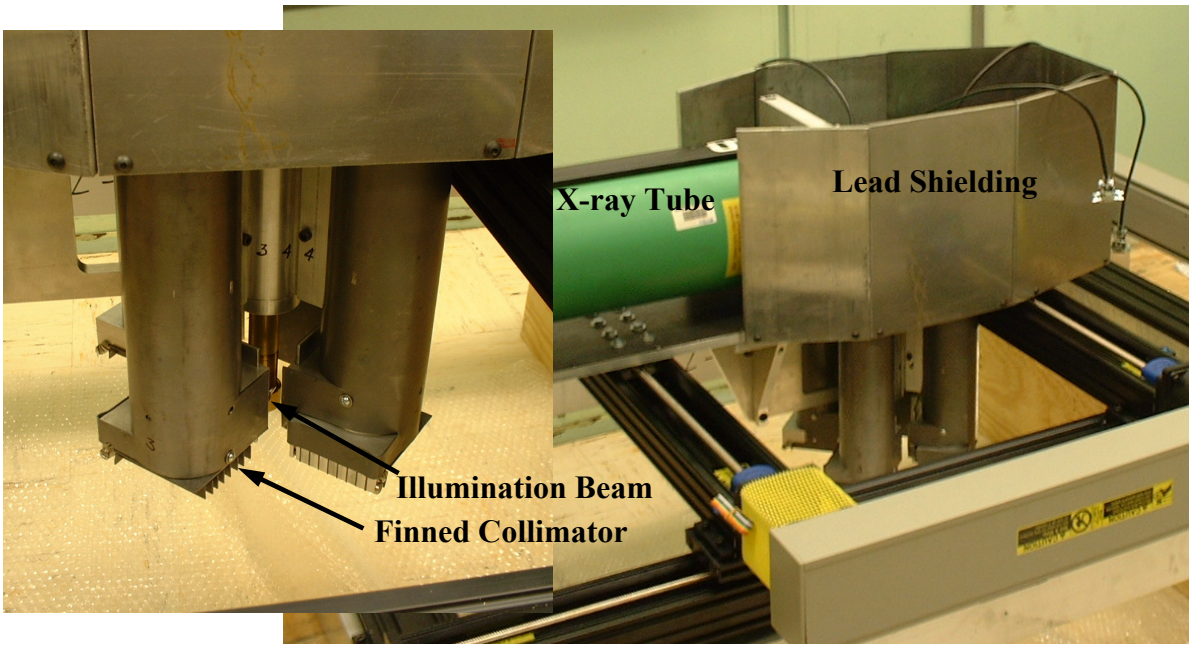

Figure 2-1. Prototype RSD scanning device built for Lockheed Martin Space Systems Co.

The x-ray tube is shielded with lead to reduce image noise. The shielding prevents leaking x-rays from the tube from reaching the detector. An illumination beam tube collimator with a small aperture shapes the illumination beam into a pencil beam for scanning. Four NaI detectors with finned collimators selectively detect backscattered photons to improve the contrast of subsurface flaws and defects. After prototype testing was completed with highly favorable

results, the design and construction of RSD scanning systems for industrial use began. RSD scanning is one of two new and/or existing NDE technologies that were chosen as favorable for detecting flaws and defects in the SOFI of the space shuttle external tank.

First Industrial Scanning Systems

Work on this dissertation begins with the first industrial RSD scanning systems. The first industrial systems had to be designed and built in a matter months, leaving little time for modeling and simulation to build an optimized system. Off-the-shelve components were chosen based on past experience and delivery lead times and then assembled in a configuration based on the success of the prototype. Figure 2-2 shows the first industrial RSD scanning system which consists of the x-ray generator, an array of detectors with their associated electronics, a scanning table, and a computer to control data acquisition, motion control, and image generation. The array of detectors is fixed to the x-ray tube and designated as the scanning head. A highly collimated x-ray beam illuminates a single pixel, and a selective backscatter field is measured by the array of detectors. Movable collimators allow each of the detectors to view a unique field. The measured signal from less collimated, or uncollimated detectors is dominated by single-collision events and contains surface and near surface information. The collimated detector can respond to single- and multiple-scatter photons which have penetrated beyond the collimation plane. When properly collimated, these photons carry information about subsurface features. Two-dimensional images are generated using a scanning pattern. For example, the scanning head will sweep from left-to-right, acquiring data and storing a line of pixels. The scanning head will then move to the next line and sweep in the opposite direction from right-to-left, obtaining the next line of data. This process is repeated, one line at time, until the entire image is completed.

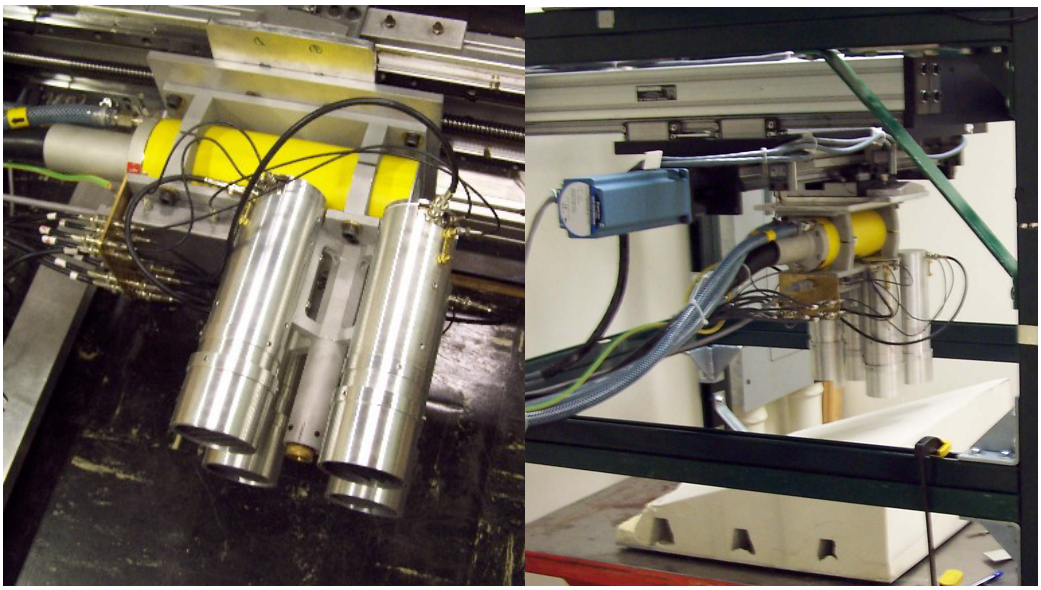

Figure 2-2. First commercial RSD scanning system configuration

Original Industrial System Component Details

The yellow cylinder in Figure 2-2 is an Yxlon MXR-160/22 x-ray generator. This is a liquid-cooled x-ray generator with a maximum tube voltage of 160 kV. However, the tube voltage is limited to 100 kV because of the 30 meter long, high-voltage (HV) cable connecting the x-ray tube to the HV power supply for the special application of scanning the external tank of the space shuttle. The x-ray tube has a maximum current of 45 mA with a 5.5 mm x-ray tube focal spot (FOC), with a 3000 watt maximum power rating. For SOFI applications, the x-ray source is nominally operated at 55 kVp and 25 to 45 mA. The four silver cylinders in Figure 2-2 are the detector assemblies. Each detector assembly includes a 5.08 cm diameter by 5.08 cm long NaI scintillator crystal, a photomultiplier tube and a custom, low-noise pre-amplifier. The collimator assembly at the end of the detector includes an array of lead collimators and the design allows for independent adjustment of the assembly in different directions. This includes in-and-out movement of the outer, circular (sleeve) collimator; in-and-out and rotational

movement of the inner collimator (collimator component with the lead fins); and in-and-out movement of the entire assembly. The collimator design provides the ability to "focus" the image by the selection of the desired scatter components. Each of the detectors generates a separate image and a cross-correlated image can also be generated from any combination of detector images. The x-ray illumination beam spot size used is typically 2 mm for first-pass scans, and 1 mm for suspect areas or areas of interest; the illumination exit beam aperture is located approximately 280 mm for the x-ray tube FOC. The beam spot for the first applications was round but customizable for different applications. The size and shape of the illumination beam is controlled by a lead insert in the bottom of the brass, lead-lined source collimator tube that extends in a direction normal to the end of the x-ray tube and is centered between the four detectors. The scanning head assembly (x-ray tube, detectors, collimators, and electronics) weigh about 29.5 kg (65 lbs). The fastest linear scan rate for this system is about 50 mm per second. For 2 mm pixels, this translates into a scanning rate of approximately 15 minutes per 0.093 m^2 (1 ft^2).

Traditional NIM-rack components were used for pulse shaping (Ortec 679 fast filter amp) and noise rejection (Ortec 850 quad SCA) before passing the digital count rate for each detector channel to the data acquisition software through a BNC 2121 interface and a National Instruments (NI) 6602-PCI counting card. A LabVIEW-based program is used to control the scanner motion, data acquisition and image generation.

CHAPTER 3
ARTIFACT AND CONTRAST GENERATION IN SCATTER X-RAY IMAGING

Contrast and Artifacts

The work on artifact and contrast generation is presented next to aid in understanding the analysis of system components in future chapters. Some of the initial foundations for this work are based on previous research.[29]

Under a simplistic CBI model, contrast is determined by changes in a scanned object's electron density and/or scattering-to-absorption ratio. While this is true for first-scatter models, multiple-scatter photons, detector collimation, and feature geometric location play a significant role in determining the relative contrast of the object and its associated features. Features with higher scattering-to-absorption ratios than their surrounding media can appear either dark or bright depending on detector collimation and feature location with respect to the collimation plane and the illumination beam. Bright veils and dark shadow effects can make a subsurface feature appear brighter, darker, or possibly even obscure the feature so that it is not visible in the image. Geometric location and orientation of the illumination beam, subsurface feature, and detectors can affect relative contrast as much as changes in electron density. Understanding how these factors affect contrast is essential to using x-ray backscatter as an imaging technique in any application.

Compton Backscatter Imaging Characteristics

Regardless of the application, the method in which subsurface features are detected is by changes in contrast with respect to the surrounding material. For gray scale images, an increase in detection rate is shown as an area of bright contrast. Likewise a decrease in signal is indicated by an area of dark contrast.

Pencil Beam, Single-Scatter Compton Backscatter Contrast

For pencil beam CBI the change in count rate or signal intensity at the detector is directly proportional to the change in contrast in the image. To understand the changes in contrast, it is important to understand the factors that affect the detector intensity. For this simplified discussion the following assumptions apply: coherent scattering is negligible and scattered photons along the incident and exit path do not significantly contribute to the detector response.

The incident attenuation factor, the probability that a photon reaches a point of interest, is given by $e^{-\alpha}$. The attenuation along the incident path for a particle of a given energy is the integral of the photon total macroscopic cross section of each material and the incident path length (r_i) to the point of interest or $\alpha = \int_i \mu(r_i)dr_i$.

Once at a point of interest, the interaction factor is the probability the photon undergoes a scattering event with an electron into the solid angle of the detector. The interaction probability factor is given by $\frac{1}{\mu_{total}}\left(\left[\int_{str}\frac{d\sigma_{KN}}{d\Omega}d\Omega\right]\frac{N_a Z\rho}{M}\right)$ where, μ_{total} is the total macroscopic scattering cross section at the interaction point, σ_{KN} is the microscopic Klein-Nishina (KN) scattering cross section, integrated over all directions in the solid angle to the detector, $d\Omega$ is the differential scattering angle to the detector, N_a is Avogadro's number, Z is the number of electrons per nuclide, ρ is the density, and M is the molar mass. The detector solid angle FOV bounds the integral, and density and material changes affect the macroscopic cross section.

After the photon is scattered toward the detector, the exit attenuation factor is the probability that it reaches the detector unattenuated. The exit factor is given by $e^{-\beta}$, the probability to of reaching the detector unattenuated. The attenuation along the exit path for a

particle at a given energy is the integral of the photon total macroscopic cross section of each material and exit path length (r_e) to the detector, $\beta = \int_e \mu(r_e) dr_e$.

The intensity of the backscattered field is affected by the combination of these three factors, incident attenuation, interaction, and exit attenuation probabilities. The probability, per source particle, that a photon has a scattering event into the detector FOV at a point is given by $(e^{-\alpha}) \frac{1}{\mu_{total}} \left(\left[\int_{str} \frac{d\sigma_{KN}}{d\Omega} d\Omega \right] \frac{N_a Z \rho}{M} \right) (e^{-\beta})$. Changes in this probability distribution are proportional to detector intensity changes. The contrast of a subsurface feature is proportional to the ratio of the intensity at the detector when the illumination beam is over the subsurface feature (I_{DF}), to the intensity at the detector when the illumination beam is not over the feature (I_{DNF}):

Contrast $\propto I_{DF}/I_{DNF}$.

This formulation implies that the contrast is not only dependent on the scanned object's electron density but highly dependant on the particle path from the illumination to the detector. Changes in contrast are due to a combination of the photon path, and the interactions along that path. Incident attenuation, interaction, and exit attenuation factors can increase or decrease the total contrast and the interplay of these factors determines the change in contrast. Without knowing specific geometric configurations and material properties, it is difficult to determine which factor will have the most effect on the contrast.

The following sections discuss how the contrast of different subsurface features change as the illumination beam moves towards, directly illuminates, and departs from the physical feature. These scenarios assume a known geometric configuration for the feature, beam and detector and that the feature is completely encompassed by homogenous materials. While this set of

scenarios is not exhaustive, it provides an illustrative foundation of fundamental scattering behavior to determine if a feature will be bright or dark with respect to its surroundings.

Void Contrast and Shadowing Effects

Many subsurface features are voids such as fuse wells in landmines, debonds, delaminations, cracks, and some types of corrosion have void characteristics. Voids can be defined as areas of substantially lower density than the surrounding material, for example, air may be considered void even in low density insulations (0.03 g/cm^3) and nylon may behave as void in tungsten. The first set of void scenarios includes voids that are above the collimation plane (CP). Voids above the CP usually result in an increase in intensity or bright contrast in an image. As shown in Figure 3-1A, as the illumination beam approaches the void region, the exit attenuation to the detectors decreases resulting in an increase in contrast. This yields a bright veil that appears between the illumination beam and the detector. Once the illumination beam is over the defect (Figure 3-1B) the intensity can further increase~~s~~ for several reasons: less attenuation for penetration below the CP, the solid angle to enter the detector increases with depth below the collimation plane, and there may be reduced exit attenuation if the return path traverses the void. As the illumination beam departs the void, the brightness can decrease due to the increased attenuation on the exit path (Figure 3-1C) and the FOV formed by the intersection of the detector and illumination beam increases with depth (Figure 3-2).

Figure 3-3 shows scenarios where the feature is below the CP. The approach, again, may result in a bright veil due to a decrease in attenuation along the exit path (Figure 3-3A). Once the illumination beam is directly over the void (Figure 3-3B), the feature can appear either bright or dark in relative contrast. The removal of a scatter source from the detection region results in the photons traveling deeper because of the reduced incident attenuation. This increases the exit attenuation and could result in a dark contrast. However, recall that the detector solid angle from

the illumination beam increases with depth (Figure 3-2), and the resulting increased interaction rate in the larger FOV of the detector tends toward a bright contrast. The interplay of these factors determines whether the void region will appear light or dark. This factor is very sensitive to relative depth below the CP. These factors may even combine in such a way to cancel, and result in no change in contrast. As the illumination beam begins to depart the physical feature (Figure 3-3C), the void should appear darker, because the exit attenuation is increased.

Scattering and Absorption Contrast, and Shadowing Effects

Whether a feature is a scatterer or absorber is determined by the surrounding material. Aluminum with respect to lead would be considered a scattering feature, but aluminum with respect to nylon would be considered an absorber. Scattering features may also be very low density compared to the surrounding materials. For low density scattering features, the void scenarios can play a dominant role in determining the feature contrast. As the illumination beam approaches scattering features that are above the CP (Figure 3-1A), the feature will increase attenuation along the exit path resulting in a dark shadow between the illumination beam and the detectors. When the scattering feature is directly illuminated and above the CP (Figure 3-1B), the feature may appear bright or dark. If the density of the scatterer is approximately the same order of magnitude or higher than the surrounding medium, then this scattering feature may act as an attenuator on both the illumination and exit path resulting in a dark image. If the scattering feature has very low density with respect to the surrounding material then it may behave as a void region and appear bright. A near perfect scatterer (scattering-to-total cross section ratio approximately one) may also cause can an increase in contrast with an LMR effect (diverged laterally-migrated scatter source). As the illumination beam departs the physical feature (Figure 3-1C), the feature will appear darker than the surrounding material, unless it is comparatively low density.

Figure 3-3 shows the scattering feature below the CP. The approach (Figure 3-3A), usually results in a dark contrast due to an increase in attenuation along the exit path. Scattering features are typically bright when directly illuminated if the scatterer consequently reduces incident and exit attenuation (Figure 3-3B). Because the scattering paths do not change as the illumination departs the subsurface feature as shown by the path of shallow scatter (there are 2 scatter paths) in Figure 3-3C, the contrast remains bright. However, if the scattering feature is very low density, then the void scenarios for contrast behavior interplay with the scattering scenarios. In these situations simulation or experimentation may be required to determine the dominate factors of contrast generation.

To predict relative contrast for absorbing features is relatively simple. The factors in play for absorbing features will always induce a dark contrast and result in a shadow between the illumination beam and the detector on approach.

Each of the scenarios for scattering, absorbing and void features is summarized in Table 3-1. Detector, collimation, illumination beam, feature geometry and relative position are extremely important in determining relative contrast for each of these scenarios. Different combinations of contrast factors and scenarios can combine in ways that make the feature contrast intuitively difficult to predict. These factors can even combine such that no change in contrast occurs. Two experiments are discussed in the following sections. The first experiment demonstrates some of the contrast scenarios discussed in the ideal situations described above. The second experiment demonstrates how inhomogeneities and complex geometry in an NDE application can make contrast changes difficult to predict.

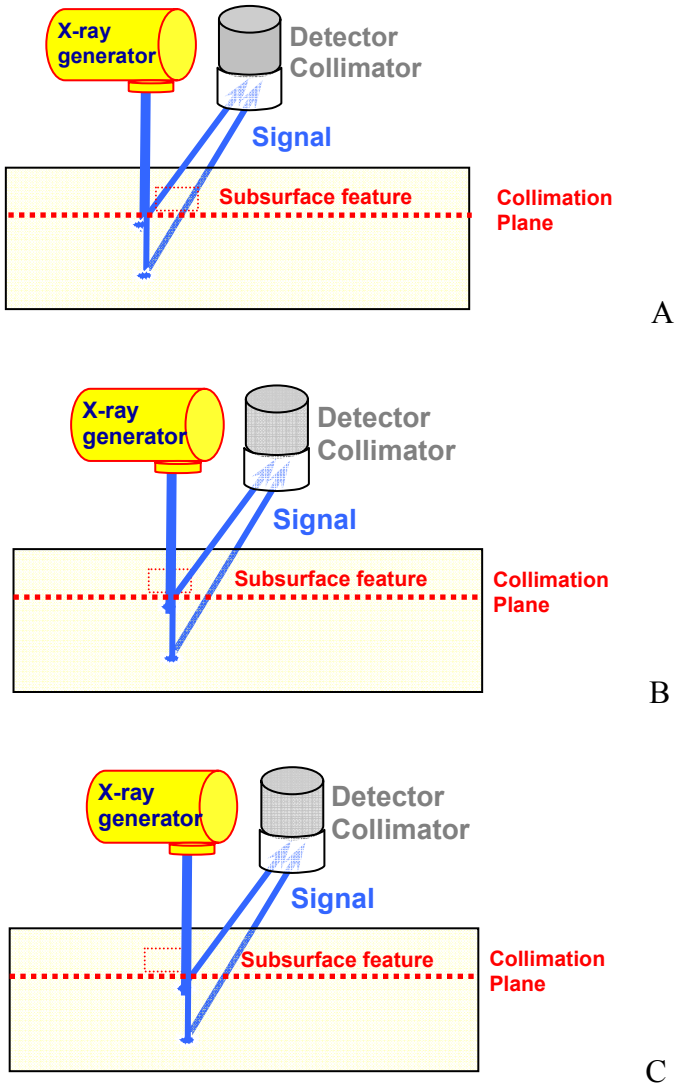

Figure 3-1. Subsurface features above collimation plane A) pre-direct, B) direct illumination, and C) departing illumination

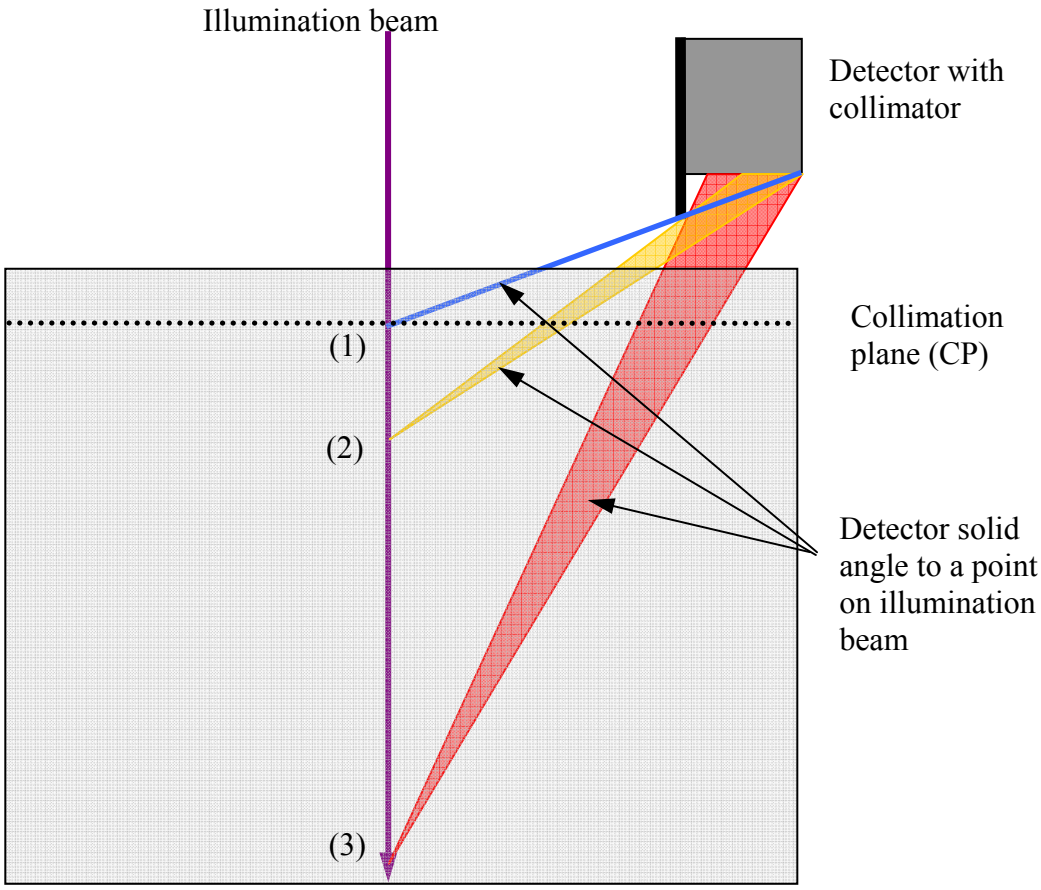

Figure 3-2. Increasing detection solid angle from points along illumination beam with increasing depth from the CP

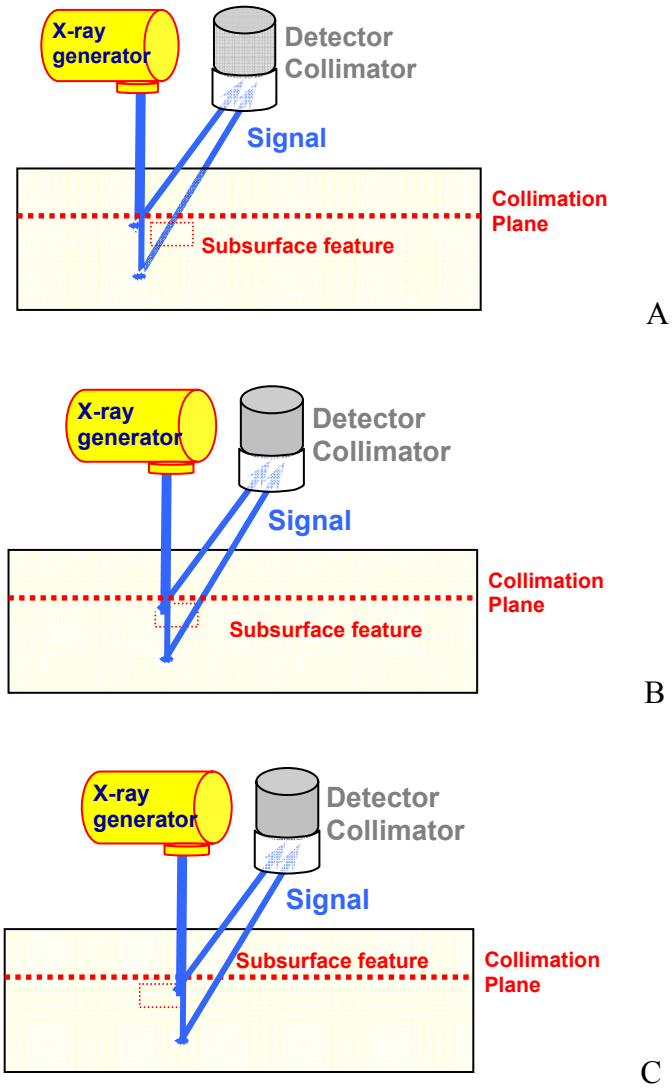

Figure 3-3. Subsurface feature below collimation plane (A) pre-direct illumination (B) direct illumination and (C) departing illumination

Table 3-1. Relative grey scale contrast table for various RSD imaging modalities based on feature type, and relative location

Relative Void						
Figure	3-1A	3-1B	3-1C	3-3A	3-3B	3-3C
Above CP[a]	x	x	x			
Below CP[b]				x	x	x
Approach[c]	x			x		
Direct[d]		x			x	
Departure[e]			x			x
Relative Contrast[f]	Bright	Bright	Bright	Bright	Bright or Dark	Dark
Relative Scatterer						
Figure	3-1A	3-1B	3-1C	3-3A	3-3B	3-3C
Above CP[a]	x	x	x			
Below CP[b]				x	x	x
Approach[c]	x			x		
Direct[d]		x			x	
Departure[e]			x			x
Relative Contrast[f]	Dark	Dark or Bright	Dark	Dark	Bright	Bright
Relative Absorber						
Figure	3-1A	3-1B	3-1C	3-3A	3-3B	3-3C
Above CP[a]	x	x	x			
Below CP[b]				x	x	x
Approach[c]	x			x		
Direct[d]		x			x	
Departure[e]			x			x
Relative Contrast[f]	Dark	Dark	Dark	Dark	Dark	Dark

[a] subsurface feature located above collimation plane, Figure 3-1
[b] subsurface feature located below collimation plane, Figure 3-3
[c] subsurface feature as illumination beam approaches, Figures 3-1A and 3-3A
[d] subsurface feature directly illuminated, Figures 3-1B and 3-3B
[e] illumination beam departing from subsurface feature, Figures 3-1C and 3-3C
[f] relative contrast in grey scale image with respect to surrounding material

Measurement Results and Discussion

The SXI RSD scanning system was used to scan an aluminum plate to demonstrate some of different contrast mechanisms and artifacts from pencil beam CBI for ideal situations. An aluminum plate (Figure 3-4) has three channels that are 10 mm wide, 2 mm high, and run the length of the 150 mm plate. The top of the channels are located at depths of 3 mm, 5 mm, and 7 mm, from left to right in Figure 3-4. The object was scanned with the illumination beam and channels parallel to detectors two and four, and perpendicular to detectors one and three (Figure 3-5). The placement of the images in Figure 3-5 corresponds to the relative detector position during the scan. The x-ray tube voltage was 75 kV, at 40 mA, with an FOC of 5.5 mm. A 1.0 mm beam aperture with 1.0 mm pixels and a dwell time of 0.1 seconds per pixel were used to acquire the image.

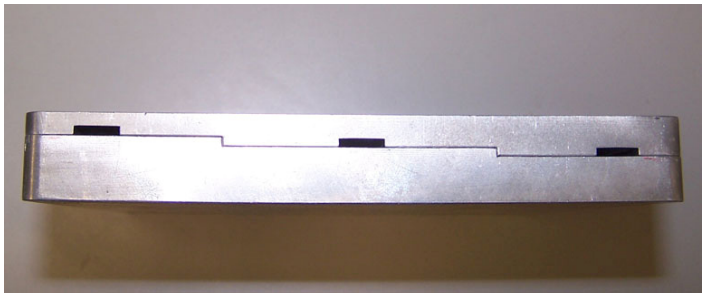

Figure 3-4. Aluminum sample plate with 10 mm wide, 2 mm high, channels at depths of 3mm, 5 mm and 7 mm from left to right

The images for detectors one and three are presented in Figures 3-5A and 3-5C, respectively. In this geometry the channel was orientated perpendicular with respect to the detector and the illumination beam. The void channels are below the collimation plane which corresponds to the scenarios in Figure 3-3. As expected a bright veil appears when the illumination beam is between the channel and the detector due to a reduced exit path (illustrated in Figure 3-3A) of the scattered photons. Note that because of the mirror symmetry of the

channel, illumination beam, and detector arrangement, the bright veil effect is mirrored in the corresponding images in Figures 3-5A and 3-5C. Direct illumination appears dark (Figure 3-3B) because a scatter source was removed from the FOV and the photons must now travel deeper and some of the exit paths may not be through the channel. Opposite of the bright veil, a dark shadow can be seen cast in the channel. This dark contrast area in the channel indicates that the exit path of the majority of photons is no longer through the channel, but through solid aluminum. This corresponds to Figure 3-3C and again, the effect is mirrored between Figure 3-5A and 3-5C.

The collimator settings and, therefore, the collimator plane for detector two are identical to collimator settings for detectors one and three. The channel is below the collimation plane. The only difference is that the channel orientation is along the same line as the illumination beam and detector. There is no bright veil (except possibly in the corners of the image) or dark shadow in this image because their production mechanism was removed. Decreased incident attenuation to a deeper point leads to an increased interaction probability (increased FOV to the detector, Figure 3-2) and feature orientation ensures decreased exit attenuation from this deeper point both contributing to a bright contrast.

Detector four is over-collimated, and the channels in the aluminum are above the collimation plane (Figure 3-1). The channel orientation is along the same line as the illumination beam and detector, just as for detector two. Because of the over-collimation (about 10 mm of collimation depth), the backscatter signal is on average 40 times lower than in the other detectors in this configuration, but the channel still appears brighter in contrast (Figure 3-5D). This is because of the reduced attenuation along the entrance illumination path and reduced attenuation along the exit path.

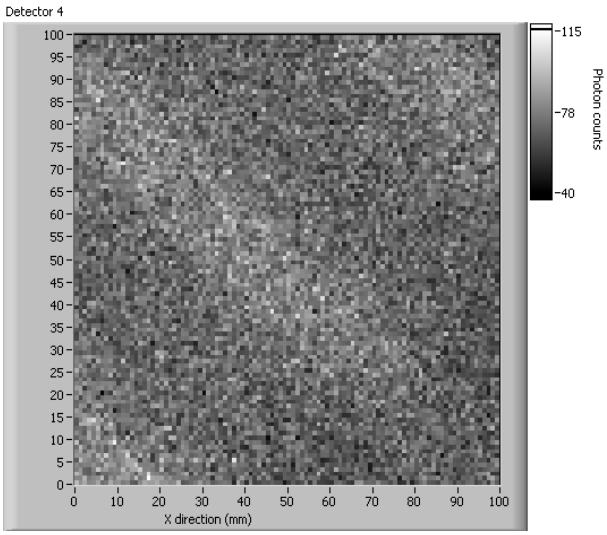

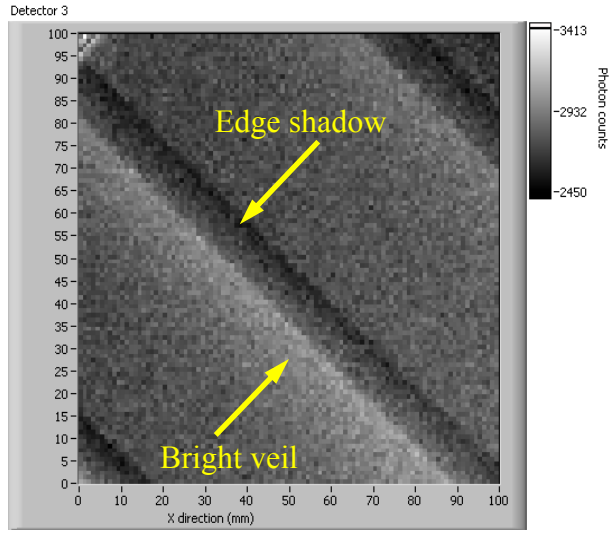

D) Channels above collimator plane. Detector 4

C) Channels below collimator plane. Detector 3

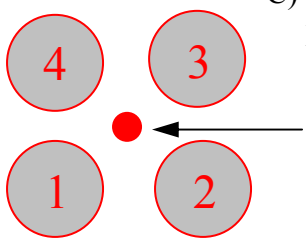

Illumination beam between four detectors

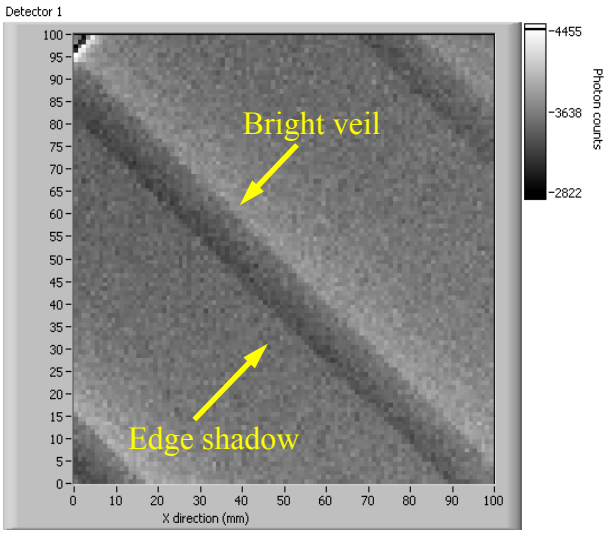

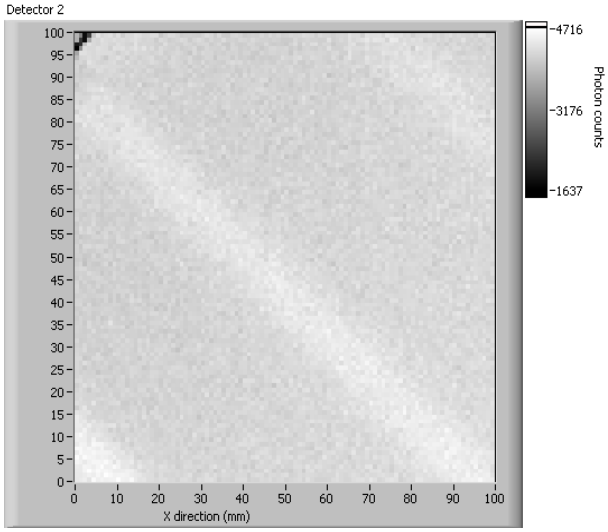

A) Channels below collimator plane. Detector 1

B) Channels below collimator plane. Detector 2

Figure 3-5. RSD image results of the aluminum plate (Figure 3-4)

Application of Contrast Mechanisms

Changing contrast mechanisms can be used to find the depth of a feature. As shown in Figure 3-6, a void is located in the gap filler material of a composite sample and the sample is on an aluminum substrate. The purpose of the inspection is to find void locations, but because of inhomogeneities and geometric configuration, the gap filler material (a scatter) controls the contrast factors. As a result, the scattering scenario logic must be applied, even though the scan is to determine void depth. A SXI RSD scan of the object was taken with the CP set to increasing depths of 3 mm (Figure 3-7A), 6 mm (Figure 3-7B) and 9 mm (Figure 3-7C). The images were obtained with a tube voltage of 60 kV and current of 45 mA, with 1 mm illumination beam and image pixels. When the scatterer (gap filler materials) moves from below the CP (Figure 3-7A), to above the CP (Figure 3-7B) the feature changes in contrast from bright to dark, thus indicating the end of filler and the beginning of the void region is located between 3mm and 6 mm into the interrogation object. The actual void region is located about 4 mm into the object.

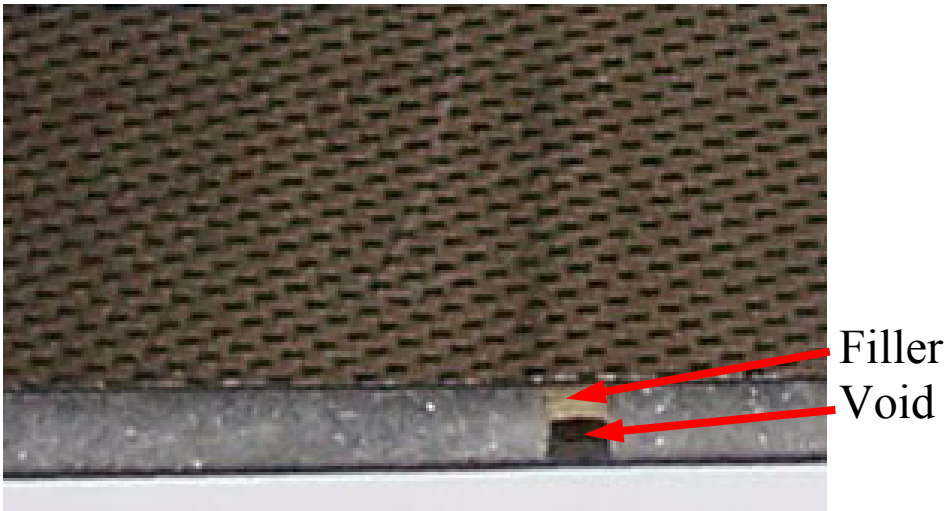

Figure 3-6. Composite material with a void region in the gap filler

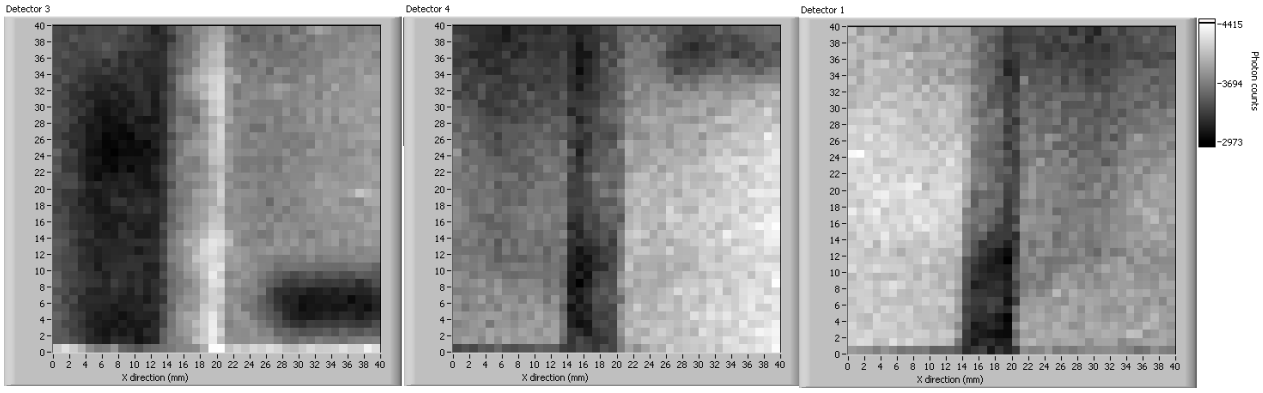

A) 3 mm CP depth B) 6 mm CP depth C) 9 mm of CP depth

Figure 3-7. RSD scanned image of a composite material with a void region in the gap filler

Conclusions about Artifact and Contrast Generation

Feature contrast in a pencil beam Compton backscatter imaging system is directly proportional to the change in intensity of the backscatter field measured by the detectors. This formulation for feature contrast implies that the contrast is dependent on the incident attenuation factor, interaction factor and exit attenuation factor. To what degree each factor contributes to the change in contrast is a function of the photon path, feature properties, and relative geometry orientation of the feature, illumination beam and detectors. The dominant factors tend to be the exponential terms along the incident and exit paths. But changes in scattering cross section, and change in solid angle, as well as the detector-, target-, feature-, and beam- relative geometry affect the interaction factor and consequently contrast. The interplay of these contrast factors determines the change in contrast in different pencil beam Compton backscatter imaging techniques such as highly collimated, uncollimated, and Radiography by Selective Detection. An understanding of these contrast factors and their interdependencies can be used not only to detect features, but to predict parameters such feature depth, size and orientation making Compton backscatter imaging a valuable single-sided imaging tool.

CHAPTER 4
OPTIMIZATION AND ANALYSIS OF RSD SCANNING SYSTEM COMPONENTS

Detector Testing

The first production radiography by selective detection system (RSD) detectors for Michoud Assembly Facility (MAF) were 5.08 cm diameter, 5.08 cm thick NaI(Tl) detectors with photomultiplier tubes (PMTs) from Bicron with a 400,000 max count rate custom preamplifier from Inspirion, LLC. One of the very first improvements to the system was to modify the time constant of the pulse preamplifier to count as quickly as possible considering the decay time constant of the NaI(Tl) crystal (230 ns). The use of this "fast" preamp enabled an 800,000 (1 MHz analog bandwidth) max count rate detector. The immediate impact was to allow the RSD scanning system to acquire data twice as fast, likewise reducing the scanning data acquisition time without increasing the statistical error in the counts. These NaI detectors are used in every RSD system with the exception of the new compact prototype system, to be discussed in Chapter 5. NaI is considered the standard scintillator to which most scintillator detectors are compared. Because of NaI detectors successful results in RSD imaging and flaw detection, it will be used as a standard for detector development benchmarking.

Comparison of NaI and plastic (BC404) scintillation

Some RSD system NaI detectors are 5.08 cm in diameter and 5.08 cm thick. Although a much thinner NaI crystal (6.35 mm thick) is adequate and provided the same quality images, 5.08 cm thick crystals were more readily available off-the-self. Plastic (BC404) scintillator detectors were tested in comparison to the NaI detectors, because plastics have a much faster decay time (1.8 ns), and could in theory measure higher radiation fields. The plastic detectors have a density of 1.032 g/cm3 and a peak emission of 408 nm.[30] The plastic detectors tested also had a 5.08 cm diameter, 5.08 cm thick active detection volume, and used about a 1 microsecond

pulse width preamplifier in count mode. However, plastic detectors were about 30% less efficient than NaI detectors. As a result the count rate on the plastic detectors was about 2/3 of the count rate of the NaI detectors. A lower count rate resulted in images with less contrast in comparison to the NaI detectors and potentially longer image acquisition times. Plastic detectors should be investigated in a current mode configuration. Because one of the inherent problems with pencil beam CBI is the source intensity limitation, work with small area plastic detectors stopped after several image measurements were taken. But, plastic detectors may still play role in SXI because of their large size, speed, availability, and ease at which plastics can shaped into optimal geometries.

Copper-doped Quartz

A copper-doped quartz scintillator material is currently being used for making dosimetry measurements in medical physical.[31] This material has physical properties such that it can be optically fused to a fiber optic cable with a high coupling efficiency; light loss at the interface coupling is less than 1%. Most of these dosimetry detectors are about 1 mm in diameter and demonstrate nominally good light output in the energy range for x-ray backscatter (40 – 80 kVp) for low Z material NDE. The success and efficiency of the these detectors led to the testing of a larger copper-doped quartz crystal, about 2.54 cm in diameter by 0.635 cm thick. It was mounted to a Hamamatsu R6095 PMT and tested. The detector response to the x-ray backscatter field was about two orders of magnitude less than for the NaI detectors, so no further testing was performed. The low response of the crystal is believed to be related to the large size of the crystal used for the backscatter application. Most of the doping material remains near the surface of the crystals. This is ideal for small detectors but not for the larger area detectors needed for x-ray backscatter imaging, because the crystal may actually attenuate the scintillation light source.

PIN-Diode Detectors

The use of PMTs along with an appropriate scintillation crystal such as NaI(Tl) or YSO provides for a very fast and high resolution detection and imaging system; however, photo-multipliers tend to be large and fragile, and usually require external biasing and shaping/amplification electronics. PIN diode detectors have the following advantages: require little or no biasing, are very small in size, and much more rugged than a PMT. The primary disadvantage of the PIN is that it lacks the signal-to-noise (SNR) of a typical PMT type detector. In an attempt to overcome this deficiently Inspirion, LLC worked on developing a new preamp.

Universal charge preamp

To improve the SNR a new preamp was designed. This preamp design is based upon a low noise, room temperature "Charge" type preamplifier, designed for pin-diode testing but universally ported over to the YSO detector, which has the following features:[32]

- Higher front-end gain for better overall noise figure
- Much lower noise front-end amplifier (FET transistor)
- Independent Mu-metal shield
- Digital baseline adjust potentiometer for lower micro-phonics
- 3rd order "T" filter for 12V input power
- Lower noise 2nd. stage amplifier[32]

This design also has some very important mechanical advantages. Primarily, the use of a solid state adjust potentiometer reduces the height of the card by 50%. The new preamp design is truly "universal", in that it can be used with both PMTs and PIN diodes. The card accepts a wide variety of PIN sizes and FET footprints to match the characteristics of different detector types and PMTs, as well as time constants.[32] In addition to pin-diode applications, the performance (gain and SNR) of the universal preamp warranted implementation in YSO detector applications.

Pin-diode test results

Only one pin-diode detector has yielded test results over the past three years. A room temperature PIN from Advanced Photonix, model SD 445-14-21-305, is coupled to a CsI scintillator, measuring 1 cm x 1 cm x 0.1 cm. The pin-diode detector operates in current mode (integral of the pulse mode). An NI-PCI-6115 A/D card was used to measure the changing voltage from the pin-diode detector. The voltage is sampled over a pixel, and an average voltage is calculated. The average voltage over a pixel is then mapped to a 16 bit integer range from 1 to 65536 and stored in a data array. The data array is a tab-delimited ascii text file, the same format as for the counting mode detectors, to allow the same LabView coding to handle image processing and generation for both current and code mode detectors for the RSD system.

An aluminum plate with five holes machined in the back side was imaged for a comparative evaluation. For a quantitative comparison, the relative contrast of each flaw is calculated with respect to the surrounding background. The relative contrast is defined as: $\mathrm{Re}\,lativeContrast = \frac{(Signal - Background)}{Background}$. A positive contrast would indicate the defect is brighter than background, likewise a negative contrast would indicate the defect is darker than the background. For the holes on the upper left of the image, the NaI has a relative contrast of -2.1% (Figure 4-1A) and the pin-diode a relative contrast of 1.4% (Figure 4-1B). The pin-diode detector has SNR 50% lower than the NaI for the images in Figure 4-1. It should be noted that Figure 4-1B is the "negative" of Figure 4-1A. The negative image is due to a coding error that used a negative slope on the mapping function when converting the voltage to a 16-bit integer range. The current mode electronics have also had issues with temperature drift, which should be resolved in the near future.

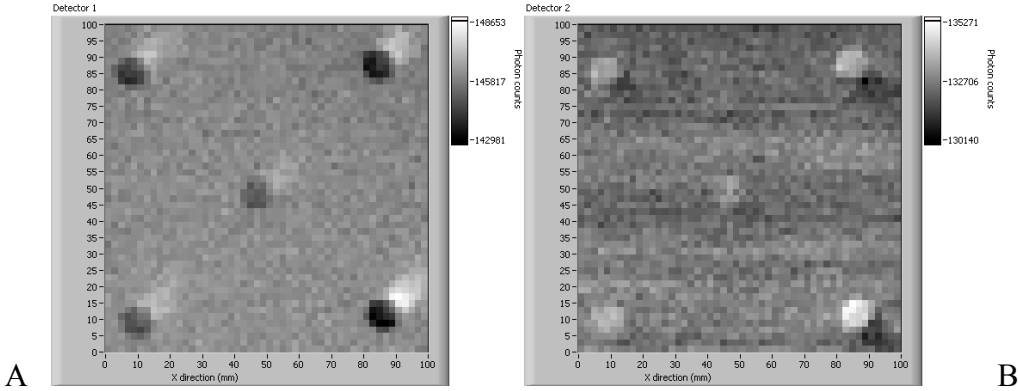

Figure 4-1. RSD image of an aluminum plate with 5 holes for, A) NaI PMT detector, and B) CsI pin-diode detector

YSO Detectors

Yttrium orthosilicate (YSO - Y_2SiO_5) is a scintillating material with nominal density of 4.45 g/cm^3. YSO has a decay time constant of 70 ns, and a light output when coupled to a PMT of 1.2 times NaI, with a peak emission of 430 nm for a mono-energetic 511 keV source.[33] YSO is not only faster than NaI, with more light output, but it is not hydroscopic and more rugged.

The first YSO detector (Figure 4-2A) used a 2.0 cm diameter, 0.635 cm thick YSO crystal. The crystal is optically coupled to a Hamamatsu R6095 PMT and a BICRON preamplifier. This detector is about 28 cm x 3.5 cm including the wire couplings and was assembled for testing purposes from surplus components. While the PMT was about 10 times noisier than the NaI PMTs, photo diode model 9266B, the relative count rate per unit area of detection surface was about equal to that of the 5.08 cm diameter NaI.

The promising count rate led to the development of a second YSO detector (Figure 4-2B). This detector uses a 2.54 cm diameter, 0.254 cm thick YSO scintillator with a Hamamatsu R6094 PMT. This detector used the same electronic components as the NaI detectors that were being used in the Lockheed RSD systems. This detector is about 18.04 cm x 3.5 cm, including the wire connections.

A

B

C

Figure 4-2. YSO detector evolution, A) First YSO prototype, B) Second YSO prototype, C) Third YSO prototype

The third YSO detector (Figure 4-2C) is a compact design. This detector uses a 2.54 cm diameter, 0.635 cm thick YSO scintillator with a Hamamatsu R1924A PMT. This crystal is thicker than the second YSO crystal, to reduce the probability of cracking the crystal (the thinner crystal was cracked during detector assembly when the detector was dropped). The thicker crystal is more impact resistant and internal self-shielding from the thicker crystal does not measurably affect the light output for RSD imaging. This detector uses the same preamplifier electronic components as the NaI detectors currently used on the RSD systems and is about 12.7 cm x 3.5 cm including the wire couplings and has a mass of 462.3 g including the collimator. In comparison, the NaI detectors currently used on the RSD scanners are about 30.5 cm x 8.26 cm with a mass of 2630 g.

Image Results Comparison for YSO Detectors

One of the objects of interests used for comparing detector results is shown in Figure 4-3. The external tank of the space shuttle is comprised of two tanks, a liquid oxygen and liquid hydrogen tank. These tanks are bolted together at a flange, a portion of which is shown in Figure 4-3. A stiffener stringer is attached to the external tank at each bolting location. The inside of the stringer is then filled with SOFI, covering the bolt. Small defects, approximately 4 mm wide, 4 mm deep, and 10 mm long were machined into the SOFI close to the underside of the bolt as shown in Figure 4-3. This area was then imaged using the RSD scanning system with both YSO and NaI detectors. The images are shown in Figures 4-4 and 4-5 respectively. Because the defect is difficult to see in print, a line profile of the area with the defect is shown to the right side of each image to further illustrate that the defect is visible next to the bolt. The relative contrast for the YSO detector is about 4.7 % and 4.5 % for the NaI detector. It is difficult to determine which detector is actually functioning better, because as demonstrated in Chapter 3, the contrast is dependent on the relative geometry, which is always different for different detectors.

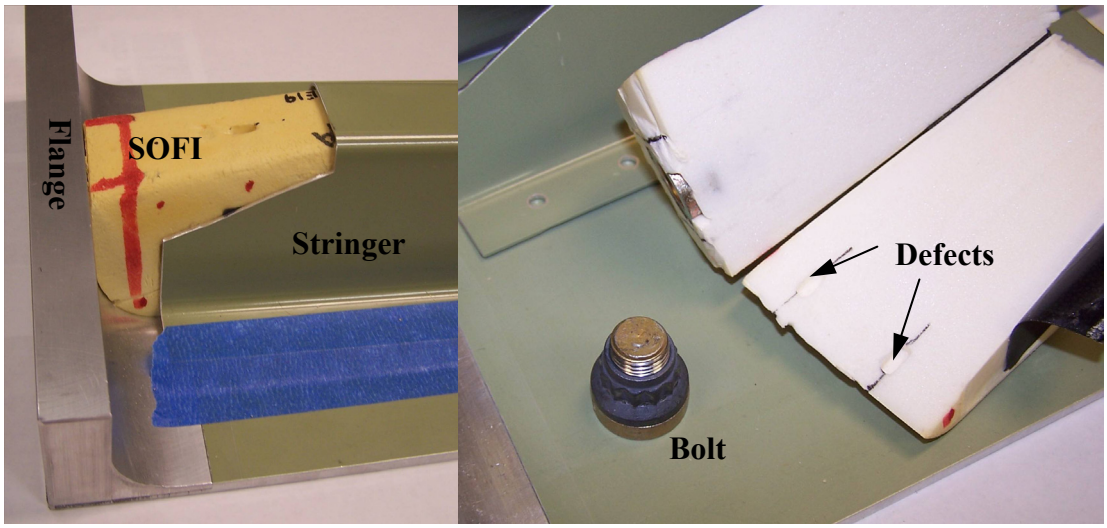

Figure 4-3. Space shuttle external tank flange bolting area with stringer and SOFI defect

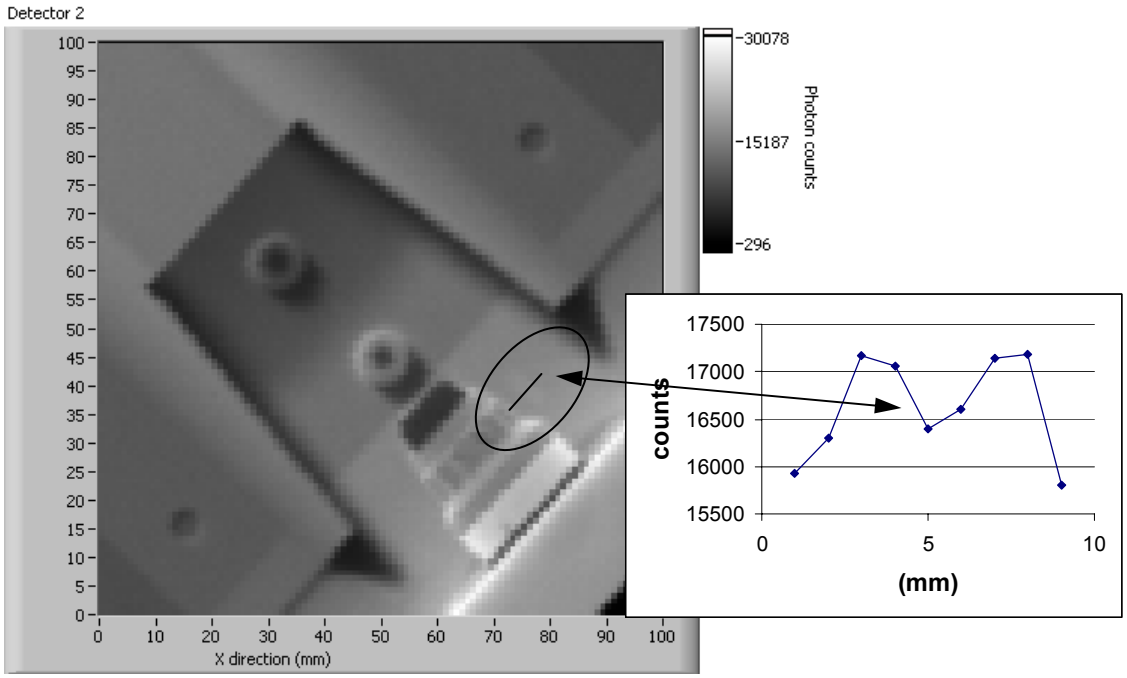

Figure 4-4. YSO, 2.54 cm diameter, detector image for external tank flange bolt near stringer with associated line profile across a known defect near bolt

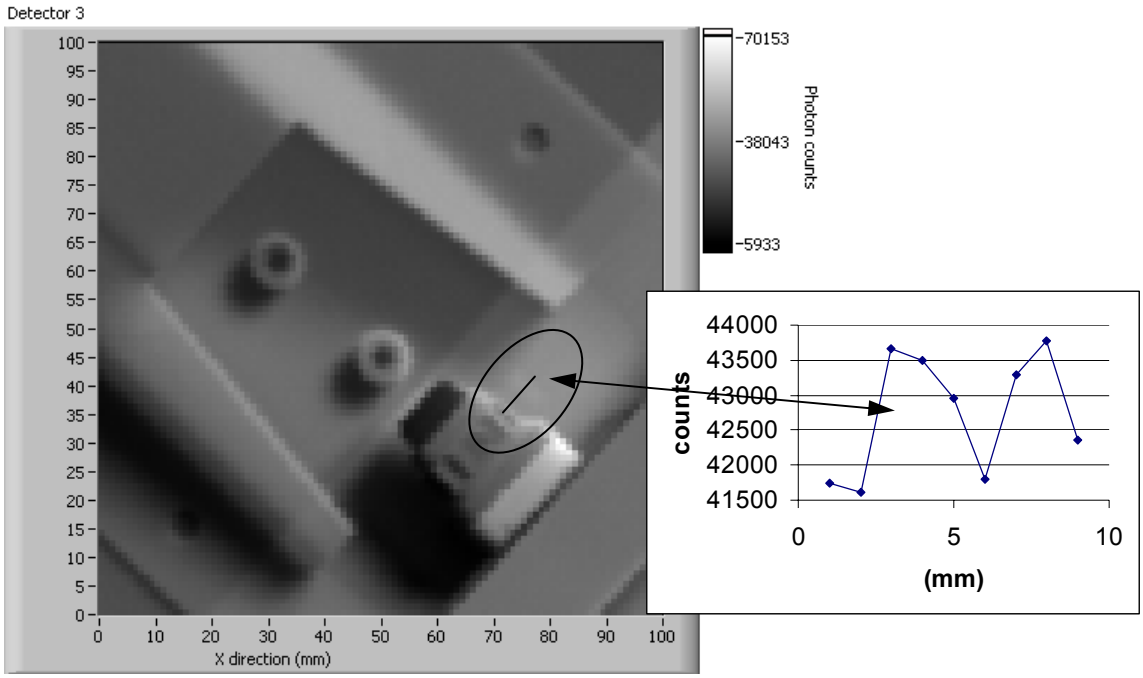

Figure 4-5. NaI, 5.08 cm diameter, detector image for external tank flange bolt near stringer with associated line profile across a known defect near bolt

RSD Scanning System YSO Detector and Preamp Upgrades

YSO detectors generate images that are on par or better than the larger NaI detectors. Over time, the YSO detector was further improved by utilizing the new universal charge preamp (see section above) to improve the SNR and a quick-connect Lemo™ connector was used to allow the HV, 12V and signal to be attached with one connector. The YSO detectors warranted implementation as an enhancement into existing RSD scanning systems at Lockheed Martin Space Systems Co., Marshall Space Flight Center, and the University of Florida. The YSO detectors mount interstitially to the NaI detectors with an orbit holder as shown in Figure 4-6. The orbit holder allows the YSO detector to be placed in any orbit position around the NaI detector, slide axially up and down, and change the polar angle with respect to the illumination beam. The 12 volt distribution box had to be modified to power up to eight detectors. The high voltage (HV) distribution box reduces the number of HV cables connected to the bulkhead. Only two HV cables are needed to power eight detectors at two different HV settings. Typically the NaI detectors are operated at 900 volts and the YSO detectors are operated at 650 volts. Figure 4-7 shows a bottom end-on view of the detectors of an RSD scanning system with all eight detectors mounted.

Addition of the YSO detectors allows the RSD scanning system to acquire data on eight independent channels. The compact size, versatility and image quality of the YSO detectors for RSD imaging set the stage for the design and testing of a compact prototype system discussed in Chapter 5.

Illumination Beam Aperture Geometry

Extending downward in a direction normal to the x-ray tube is the illumination beam collimator. The illumination beam size and geometry can be varied by changing a lead disk aperture where the x-ray beam exits the collimator tube. Originally, circular apertures were used

to illuminate a single pixel (Figure 4-8A). However, image pixels are square and a square aperture increases the illumination beam intensity by a factor of $4/\pi$ (1.27 times). The larger beam area and intensity results in a higher count rate, and reduces image acquisition time. Also note, the illumination beam is chosen slightly smaller than the pixel area (Figure 4-8A). For example, to generate an image with 2 mm pixels, it is recommended to use a 1.5 mm aperture. This reduces pixel cross illumination due to beam dispersion and helps to improve image quality. Figure 4-8B quantifies the illumination beam dispersion at 101.6 mm from the beam exit aperture. A pixel size of 2.5 mm for a 2.0 mm aperture reduces pixel cross illumination to less than 5% for a round aperture and to less than 7% for the square aperture. A scanned image of film exposure used to generate each plot is shown in the legend of Figure 4-8B. To ensure the film is not over exposed, several exposures were made at 55 kVp. The x-ray current and exposure were reduced until the beam plateau dropped below 255 (pure white in an 8 bit grey scale image). The final x-ray generator settings for the film exposures were 55 kVp, with a 1 mAs second exposure.[34]

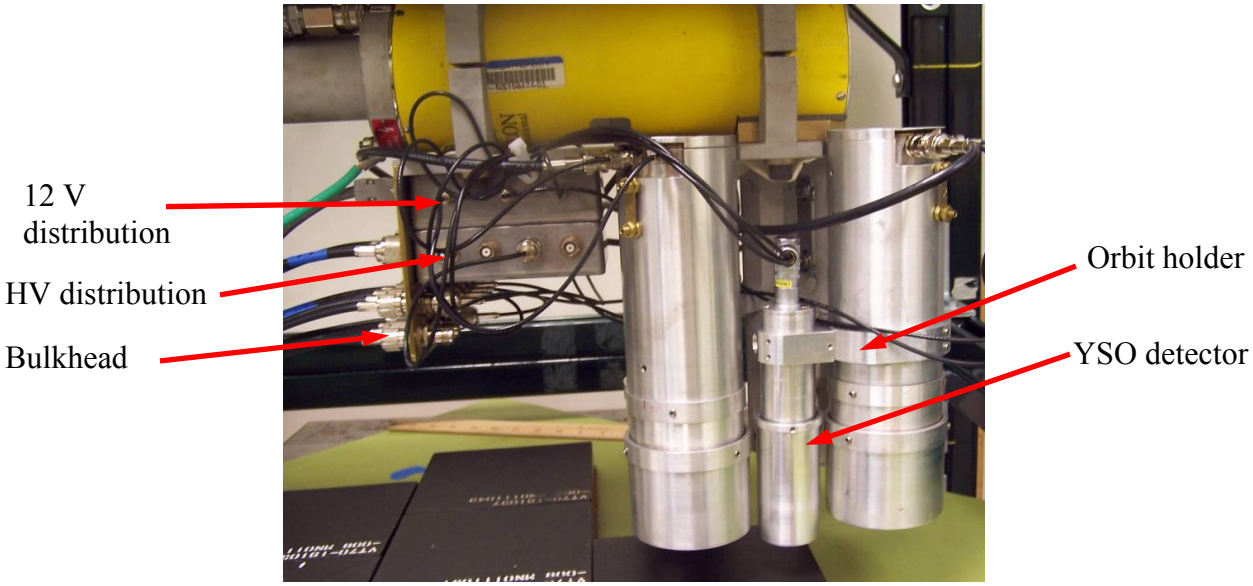

Figure 4-6. YSO detector with orbit holder, new bulkhead, new high voltage distribution box, and modified 12 volt distribution box.

Figure 4-7. SXI RSD scanning system with YSO upgrade

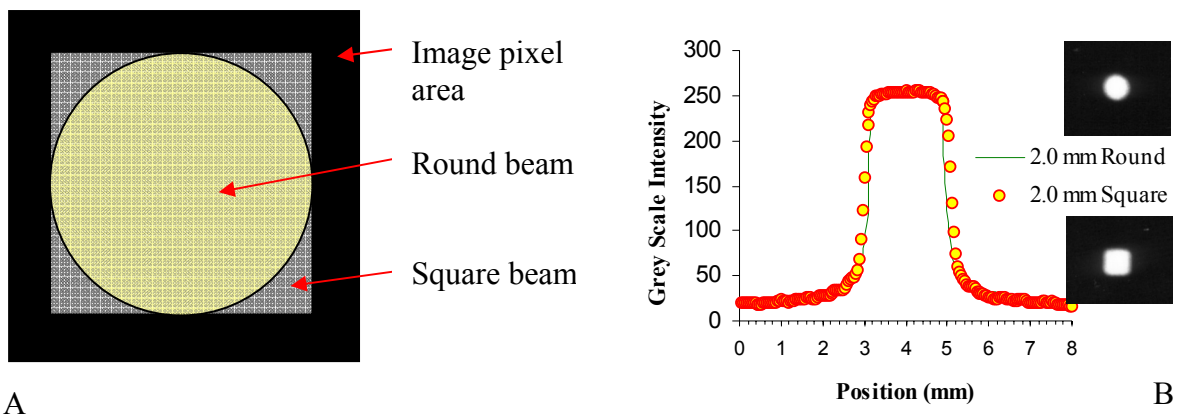

Figure 4-8. Illumination beam spot size analysis, A) Illumination beam relative aperture geometry for round and square illumination beams B) Beam dispersion measure 101.6 mm from aperture

Round and Square Aperture Image Analysis

Figure 4-9 is a picture of the layout used to scan a ramp panel with natural defects and debris embedded in the SOFI. The image pixel size is set at 2 mm, with a pixel dwell time of 0.1 seconds per pixel. The x-ray generator settings were 55 kVp, and 45 mA with a 5.5 mm FOC. The collimators extend a total of 15 mm past the surface of the NaI detectors, and the minimum separation distance (where foam is thickest) between the SOFI and the face of the detectors was 40 mm. The foam varies in thickness from 38.1 mm to 228.6 mm. The aluminum flange runs

the length of the panel and is used to bolt together the liquid hydrogen and oxygen tanks comprising the shuttle external tank. The stiffener-stringers lay perpendicular to the flange located in each position where the flange is bolted together.

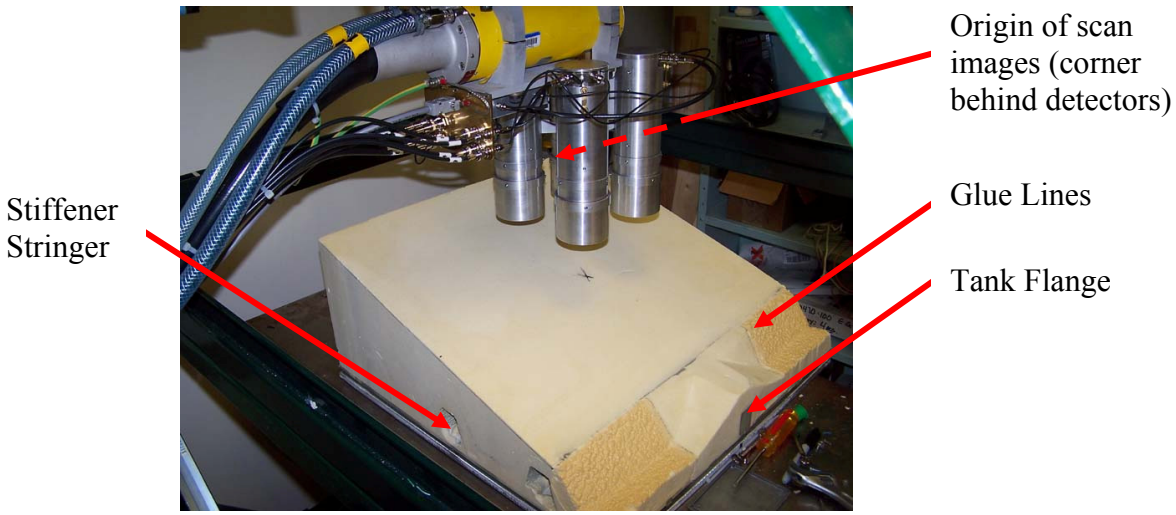

Figure 4-9. Scanning configuration for ramp panel

Figures 4-10 and 4-11 are RSD images of a ramp panel using a 2 mm round and square aperture, respectively. The difference in count rate is because of the change in area of the illumination beam aperture as shown in Figure 4-8. The average count rate for the square aperture image is approximately 1.3 times the count rate of the round aperture image as expected.

Two metal flanges run vertically in the image at x = 250 mm and are bolted together. The stiffeners are in the x-direction on both sides of the flange located at y = 100 mm, 275 mm and 460 mm. The stiffeners are bolted to the aluminum substrate. Glue lines can be seen running vertically in the image at x= 125 mm and x = 375 mm. There are five dominate natural defects in the image: defect 1 (x = 60, y = 375); defect 2 (x = 90, y = 180); defect 3 (x = 450, y = 375); defect 4 (x = 150, y = 15); and defect 5 (x = 400, y = 25). There are four items of foreign object debris (FOD) easily visible in the image: debris 1, tape (x = 175, y =180); debris 2, pencil (x =

250, y =375); debris 3, nylon washer (x = 350, y =375)**;** and debris 4, bolt (x = 360, y = 165). The count rate in the images has a decreasing trend from bottom to top due to the decreasing thickness of the foam.

The images in Figures 4-10 and 4-11 were acquired using round and square apertures equal to the image pixel size (2 mm). This example demonstrates how aperture size can affect image contrast. The absolute signal-to-background contrast for natural defect 4 is 5.2 % for the round aperture, and 4.0 % for the square aperture. The reduction in image contrast can be partially attributed to pixel cross illumination. The illumination beam aperture should be slightly smaller than the image pixel size for square apertures, and smaller or equal size for round apertures.[34]

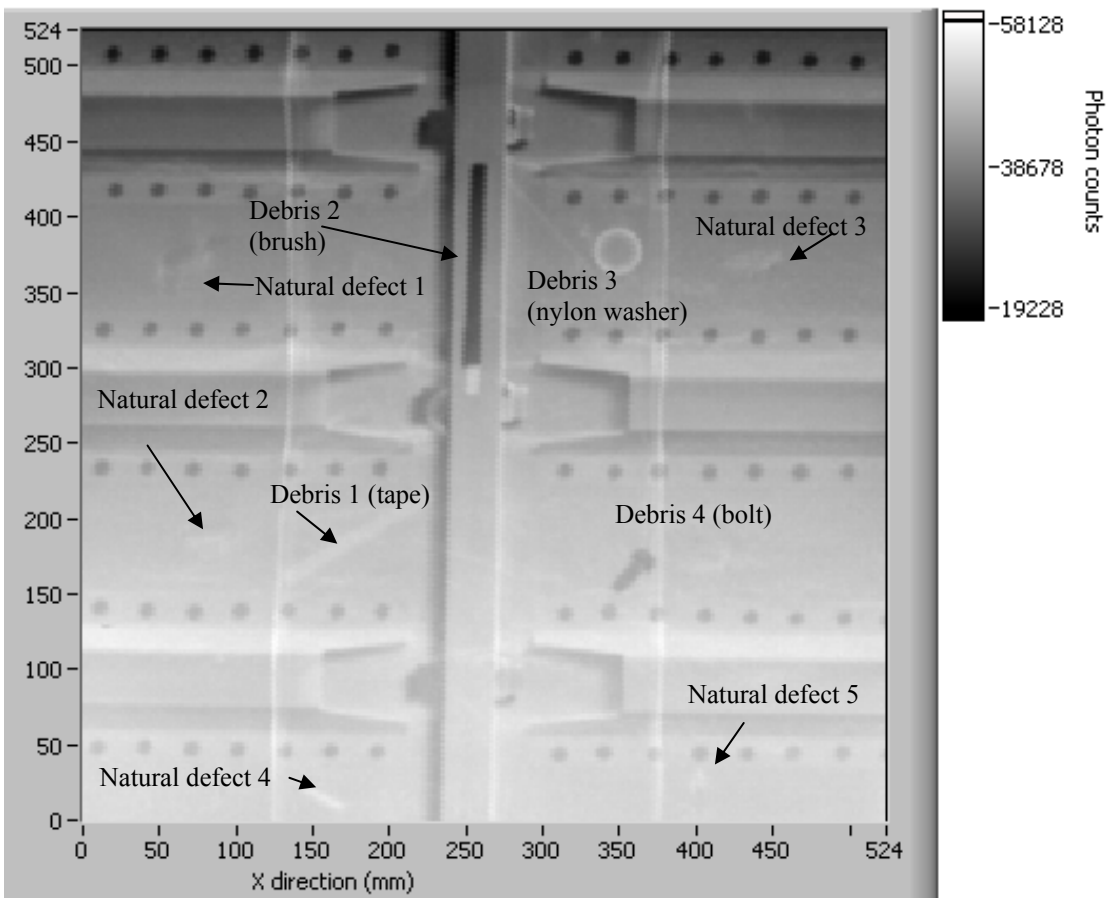

Figure 4-10. RSD image, 2 mm round aperture ramp panel image (55 kVp)

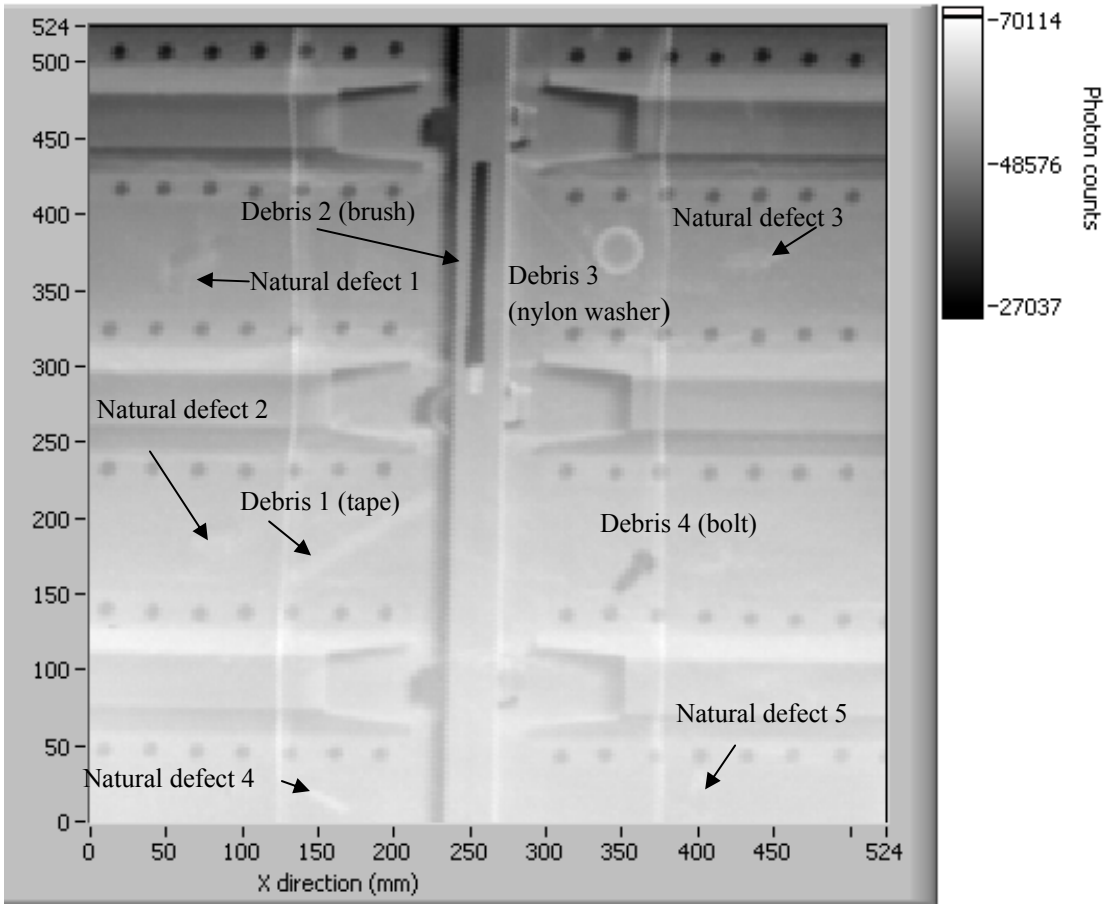

Figure 4-11. RSD image, 2 mm round aperture ramp panel (55 kVp)

Detector Modes of Operation

The University of Florida (UF) x-ray backscatter RSD system currently uses scintillator detectors. Scintillator detectors detect ionizing radiation through energy deposition into a crystal resulting in the excitation of electrons. As these electrons return to a ground state, photons in the visible light spectrum are released. The number of photons created is proportional to the amount of energy deposited in the crystal. The photons are collected by a photocathode resulting in electrons passing into the photo multiplier tube (PMT). The amplified current of electrons from the PMT can then be measured in either pulse (counting) or current (integrating) mode.

Count Mode

For count mode detectors there is a preamp connected to the signal from the PMT. This preamp has an RC circuit for collecting the charge from the PMT. The time constant for the RC circuit needs to be long enough to collect the photons and resulting charge from an interaction event, but short enough to distinguish between individual radiation interaction events. If the count rate becomes too high, it becomes impossible to distinguish between individual radiation interaction events and pulse-pileup occurs. This saturation can occur anywhere from the scintillator itself, through most stages of the electronics.

Because the number of photons created in the scintillator are proportional to the amount of the energy deposited in the crystal, and the amplification and collection process is nearly linear, the resulting height of pulses from the preamplifier are proportional to the energy deposited. Using a count rate detector allows spectroscopy or acquisition of energy with each count. The current x-ray backscatter RSD system does not analyze the pulse height, but simply counts. A pixel's contrast is proportional to the number of counts received in each pixel. Each count is equally weighted regardless of the energy of the x-ray being detected. It is possible to store the energy of each count received for an image using a very fast multi-channel analyzer (MCA); however, a 600 cm by 600 cm image with 1 mm pixels and energy data would require approximately 5 GB of disk storage.

Current Mode

In situations where the detected count rate is high so that pulse pile up occurs, current (or integral) mode can be used. In current mode, pulses are collected and integrated over a period of time, the integration response time. The response time of the circuit is large compared to the time between individual events and as a result the ability to distinguish between individual interactions is lost. The analog voltage/current from the integrated signal varies with both

detection rate and deposited energy. Typically current mode operation is only used when the radiation field is too high to count, but for RSD imaging, there is an added benefit to current mode.

To incorporate spectral energy weighting into the image contrast, either the pulse height of every individual event could be recorded in-situ or the detector can be operated in current mode. Recording the pulse height of each individual event in-situ can be costly in terms of hardware and disk storage and even very fast multi-channel analyzers are limited in rate to around 1 Mhz. Current mode offers an alternative solution, because analog voltage from the current mode detector increases with both count rate and energy, higher energy x-rays will cause the voltage to increase. If the varying voltage levels are mapped to contrast levels in pixels of an image, the contrast will be weighted toward the higher energy x-rays as shown in Figure 4-12. Each of the spectral energy curves shown in Figure 4-12 has the same number of total counts under the curve. If the contrast for the pixel was generated using count mode, there would be no difference in the contrast values for the pixel for the different spectra. However, in current mode, because the contrast is weighted by both energy and count rate, the spectral curve with the higher energy x-rays has a higher contrast value in the pixel.

Higher energy x-rays have a different scattering history compared to lower energy particles. In some cases these higher x-rays may have penetrated deeper (spectral hardening with depth penetration) or have a higher probability of interacting with the subsurface feature of interest. If this is the case, then weighting the contrast based on energy can improve the ability to detect certain features.

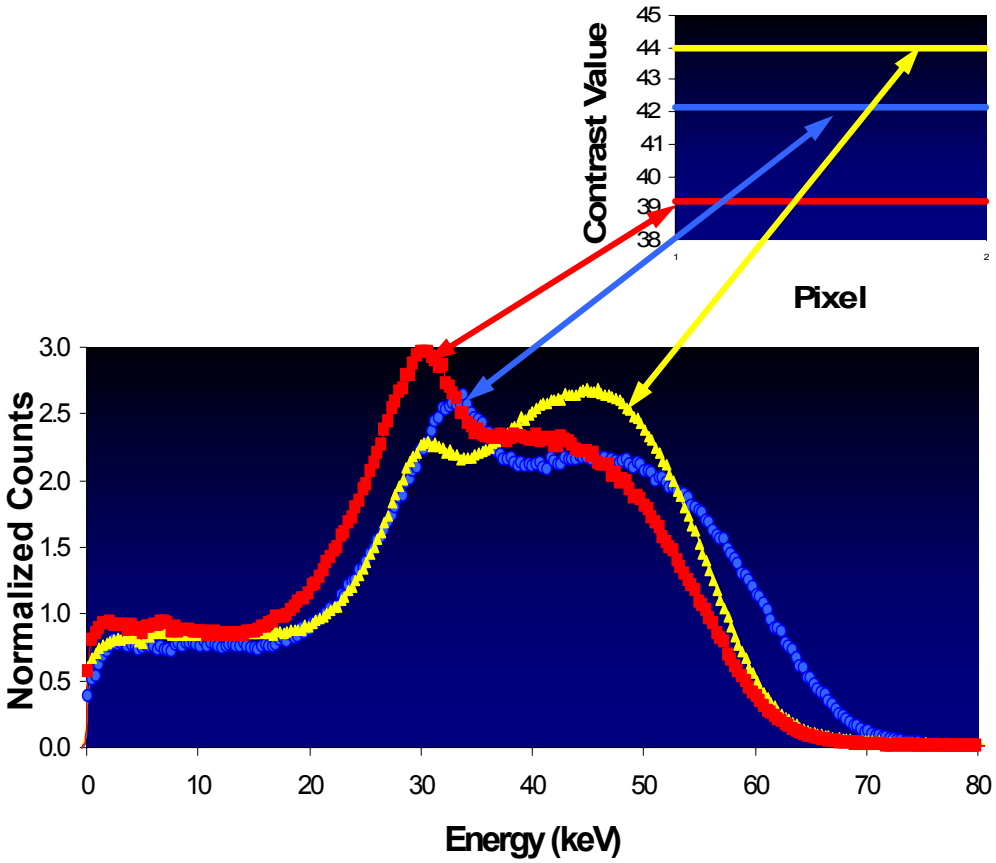

Figure 4-12. Energy weighted current mode contrast for a single pixel for varying spectral curves

Current Mode versus Counting Mode Detectors Measurements

Current mode detectors generate an analog voltage/current output that is proportional to the count rate and energy deposition, while count mode detectors generate a voltage pulse for which the height of the pulse is proportional to deposited energy. However, for the RSD scanning system, image pixel contrast was generated based on count rate for the counting detectors, and each count was equally weighted regardless of pulse height. An image data file simply consists of an array of integers (counts per pixel). The range of integer numbers is then linearly scaled to a 16-bit range (0 to 65,535) where the lowest count is mapped to zero and the highest count is scaled to 16-bits minus one. When a detector is operating in current mode, the RSD scanning

system measures the analog voltage signal, the 0 to 5 volts signal is then linearly scaled to a 16 bit range. When measuring the analog signal, the image contrast is affected by the energy of the radiation that is incident on the detector. As a result, the image contrast is weighted toward higher energy backscatter x-rays, because higher energy x-rays induce a higher voltage, but not a higher count rate. Figures 4-13A and 4-13B are SOFI calibration block images. There are two small cylindrical voids, 6.35 mm in diameter and height, and two large cylindrical voids, 12.7 mm in diameter and height. The shallow voids in the bottom of each image are located under 50.8 mm of foam and the deeper voids are near the aluminum substrate beneath 203.2 mm of foam. Absolute percent signal contrast between the void and background was calculated for the 12.7 mm voids. For the large shallow flaw, the defect-to-background is -5.7 % for current and -4.0 % for pulse mode. For the large deep flaw the respective current and pulse mode contrast ratios are -3.2 % and -2.0 %.

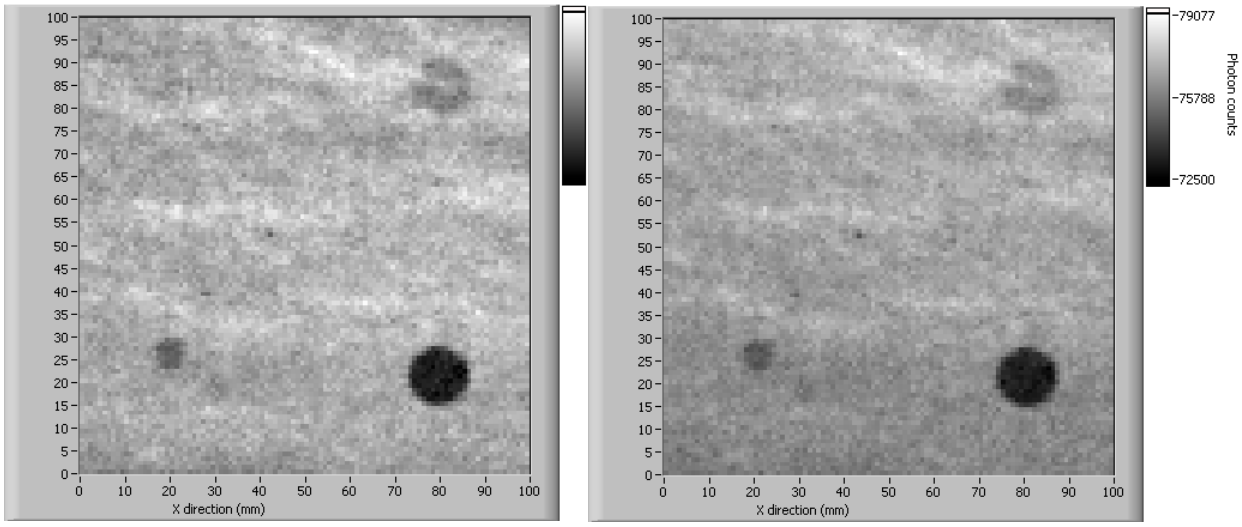

A B

Figure 4-13. RSD image of SOFI calibration block, A) current mode, B) count mode

Monte Carlo Simulation of Current versus Count Mode for SOFI

The acquired RSD images (Figure 4-13) show a difference in contrast between the current and count mode for the same detector. An MCNP[35] simulation was performed to identify the reason for the change in contrast between the two detector modes of operation. Figure 4-14 is a yz-slice of the model showing the material distribution. The NaI detector is 5.08 cm in diameter and 5.08 cm high surrounded by a 0.1 cm thick cylindrical lead collimator. The lead collimator extends 1.27 cm below the face of the detector. The separation distance between the edge of the collimator and surface of the SOFI is 5.08 cm. The SOFI is 20.32 cm thick, divided into four, 5.08 cm layers, the top, Layer 1, and the bottom, Layer 4. The aluminum substrate is 0.318 cm thick.

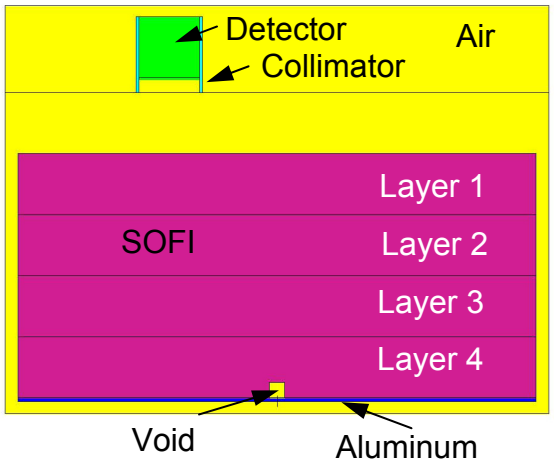

Figure 4-14. MCNP model of SOFI with aluminum substrate

Three models were used: one with no void, one with the void defect located on the bottom of Layer 4 (Figure 4-14), and one with void defect located on the bottom of Layer 1. The "void" region was 1.27 cm in diameter and 1.27 cm high (0.5 inch right circular cylinder) and filled with air. The composition of the SOFI is proprietary, but was estimated from a 50/50 combination of isocyanate and polyol with a CFC-11 blowing agent. The polyol also contains a phosporphus

flame retardant, bromine flame retardant, silicon surfactant, with an amine, tin, and potassium catalyst. The simulated SOFI was estimated to contain predominantly carbon and hydrogen, with smaller amounts of oxygen, nitrogen, fluorine and chlorine with a nominal density of 0.03 g/cm^3. The source spectrum used for the simulation was 55 kVp spectrum generated from an attenuated Kramer's spectrum for an electron beam on a tungsten target.[13] There is no source of characteristic x-rays peaks in the 55 kVp spectrum for a tungsten target with a beryllium window.

Current mode versus count mode results

A positive partial current (J+) tally with 5 keV energy bins was used to determine the backscatter x-ray spectrum entering the detector. Surface flagging was used to bin the J+ spectrum by depth penetration into the SOFI. Figure 4-15 shows the average spectrum entering the detector as a function of depth penetration. As expected the spectrum hardens (becomes weighted toward the higher energy) with increased depth penetration. The average spectrum returning to the detector from Layer 1 of the SOFI is 31.0 keV and 34.2 keV from the aluminum substrate. The void region is located just above the aluminum substrate in the bottom of Layer 4 (Figure 4-14).

The detector's count and current mode response were determined using a J+ and deposited energy tally respectively. The relative contrast ((signal – background) / background) was determined by comparing the detector's response with and without the void defect. Table 4-1 shows little change in contrast between current and count mode for the shallow void. However, for the deep void on the aluminum substrate, a change in spectrum average energy of 4.2 keV is enough to result in a change in contrast from -1.09 % to -1.27 % between count and current mode. Current mode increases the contrast of the deep void region without compromising the contrast the shallow void. The modeling results confirm the contrast trends shown in the

experimental results of Figure 4-13. Inhomogeneities, and the subjectiveness of selecting the contrast region-of-interest (ROI) for the measured image are the major contributing factors to difference between the measured and calculated results.

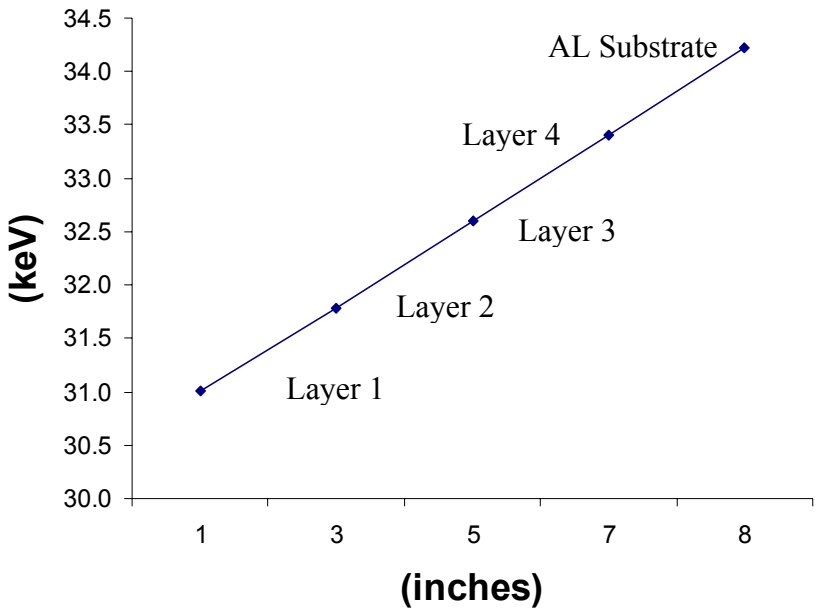

Figure 4-15. Average photon energy at detector entrance window as a function of depth penetration

Table 4-1. MCNP results comparing relative contrast for count and current mode detector operation

	Shallow (%)	Percent Error (1σ)	Deep (%)	Percent Error (1σ)
Relative Contrast Current Mode	-5.88	0.003	-1.27	0.003
Relative Contrast Count Mode	-5.82	0.035	-1.09	0.033

NaI performance

Sodium-Iodide detectors were selected for the Lockheed RSD scanning system because of their availability. In addition to examining the effect of current and count mode on image contrast, the performance/efficiency of NaI for x-ray backscatter was also analyzed. The detector absorbed fraction, absorbed photons divided by incident photons, is compared to the

average spectrum at the detector in Figure 4-16. The lowest detection efficiency, 82 %, for NaI is located around the 30 keV backscatter spectral peak. Figure 4-17 is the photon cross section scattering-to-absorption ratio of NaI as a function of energy.[36] Scatter in NaI crystal peaks at energies just below the k-edge absorption of iodine at 32 keV, severely decreasing the detectors efficiency around this energy. For low energy x-ray backscatter applications (under 70 kVp), detectors with iodine should probably be avoided. Other scintillators such as YSO have been demonstrated to be suitable replacements for NaI.

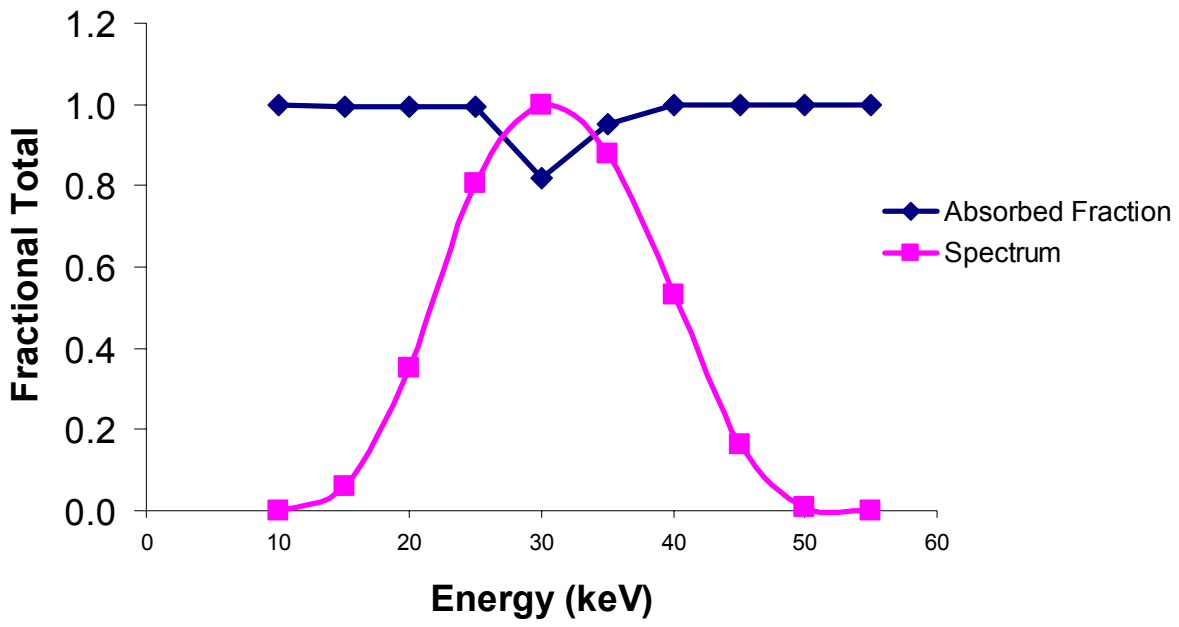

Figure 4-16. Normalize backscatter spectrum at the detector entrance window compared to the fraction of incident particles per unit energy absorbed in the detector

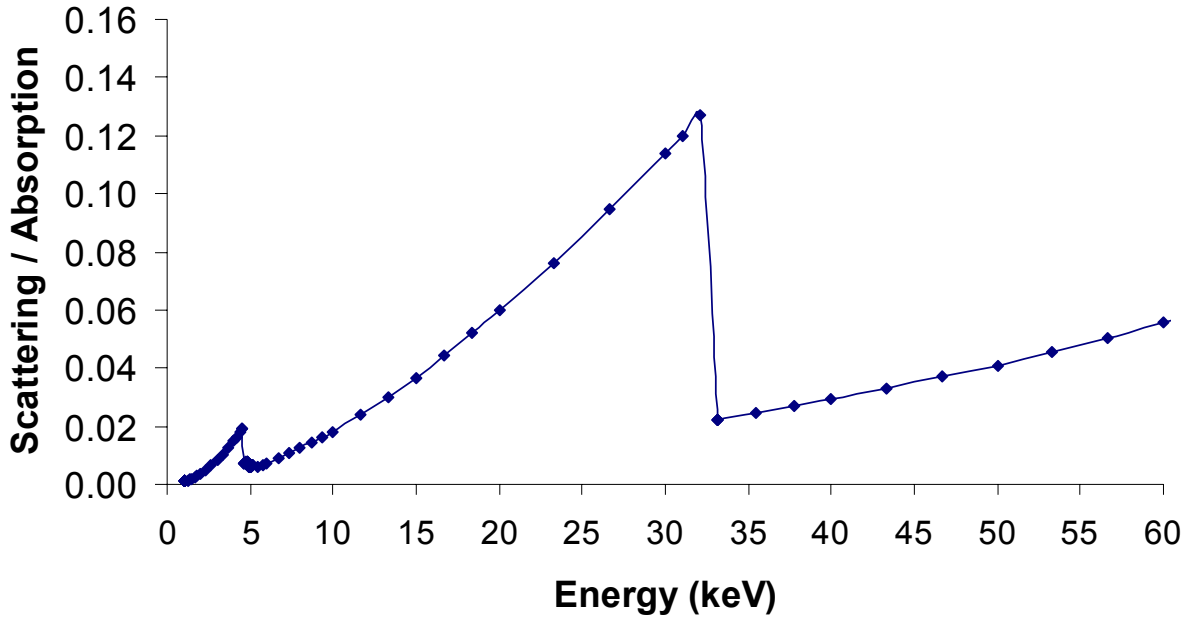

Figure 4-17. Scattering to absorption ratio as a function of energy for NaI

CHAPTER 5
RSD COMPACT SYSTEM PROTOTYPE

X-ray Tube Technology

In mid-2005 YXLON released the YXLON.TU 100-D02 x-ray tube (Figure 5-1). This x-ray tube is about 7 cm in diameter, 26.7 cm long and weighs in at about 6 kg. The YXLON/Comet MXR 160/22 tube in comparison is 10 cm in diameter, 27.9 cm long and weighs about 8 kg. Both tubes have a 1 mm (using standard acc. EN12543) electron focal spot (FOC) with a 640 watt rating. The smaller tube is limited to 100 kVp, while the large tube is rated for 160 kVp. For most low Z applications, 100 kVp is more than adequate. There is also a difference in power rating for the larger FOC on each of the tubes. The 5.5 mm FOC is rated for 3000 W on the 160 kVp tube, and the 3.0 mm FOC on the smaller tube is rated for 1500 W. The compact YXLON.TU 100-D02 tube uses the same HV socket cable as the larger 160 kVp Comet, making the tubes interchangeable between systems without having to change, HV cables, HV supply, or x-ray controller units.

Figure 5-1. YXLON.TU 100-D02 x-ray tube for testing of compact system components

RSD Scanning System Compact Prototype

Figure 5-5 is the assembled compact prototype system. Although not a final design, the compact system demonstrates the feasibility of a smaller, lighter system that delivers the high quality RSD images. The entire system weighs just over 11.3 kg (25 lbs) and is about 35.5 cm long, 15 cm wide and 15 cm high. Some of the system components are listed below:

1. Bulkhead connection to relieve strain on the signal cables
2. YXLON.TU 100-D02 x-ray tube 100 kVp max output
3. High voltage and 12 volt power distribution box
4. 2.54 cm diameter, 0.635 cm thick cylindrical YSO crystal coupled to a 2.54 cm diameter photo-multiplier tube (PMT)
5. 2.54 cm by 5.08 cm, by 0.635 cm rectangular YSO crystal coupled to a 2.54 cm diameter PMT
6. Preamplifier and detector electronics box
7. Detector mounting/guide track allowing detectors to slide along the x-ray tube
8. Illumination beam collimator tube and illumination aperture

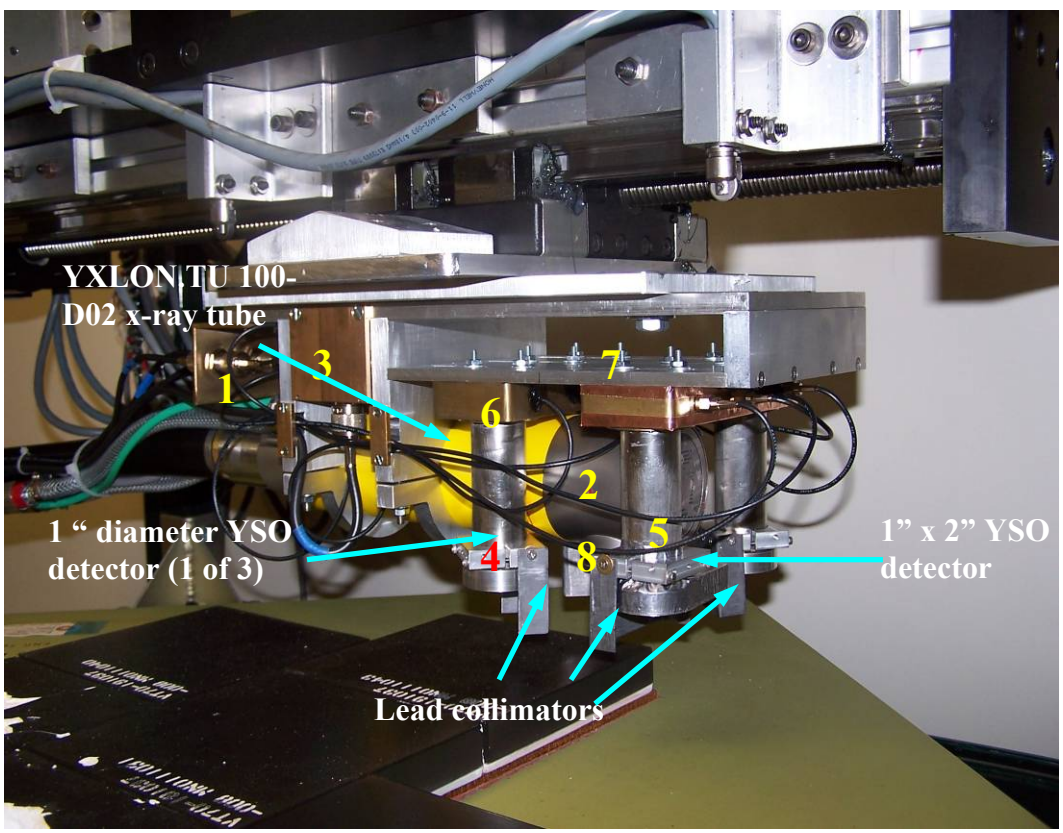

Figure 5-2. Prototype compact RSD scanning system

Compact RSD Scanning System Features

As shown in Figure 5-3, the illumination beam tube is positioned interstitially between the imaging detectors. The focal spot (FOC) of the x-ray tube is located in the direction normal to the illumination beam tube aperture near the cross sectional mid-plane of the x-ray tube as labeled in Figure 5-3 (red dot on the side of the x-ray tube housing). The x-ray tube is bracketed to the scanning head assemble with four bolts, allowing the tube to easily be rotated or removed. Two detectors are connected to each preamp housing, which can slide along a slotted positioning plate, allowing the detector separation distance from the illumination beam to vary. Figure 5-4 demonstrates how a rectangular detector can be fastened to the PMT housing, increasing the detection area from 5.06 cm^2 to 12.9 cm^2, 2.6 times.

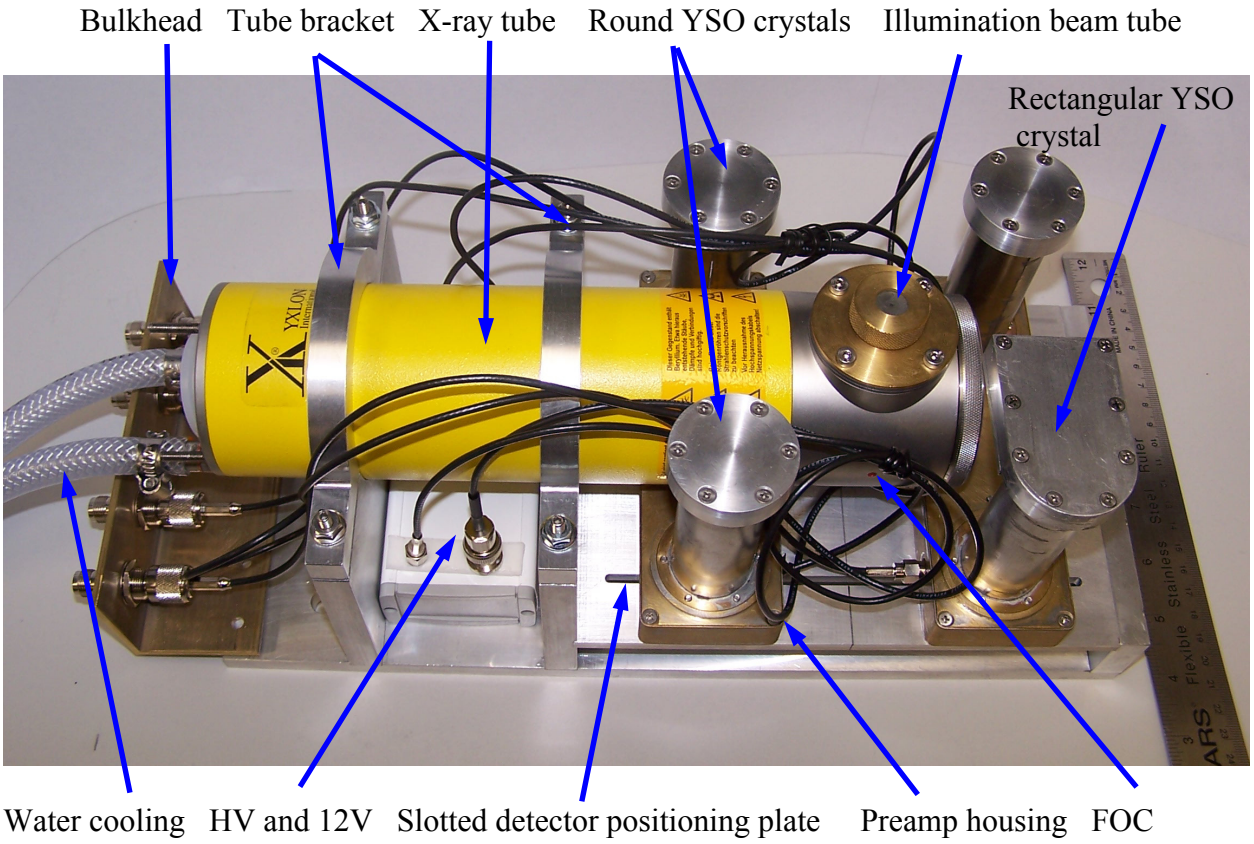

Figure 5-3. Prototype compact RSD scanning system, bottom view

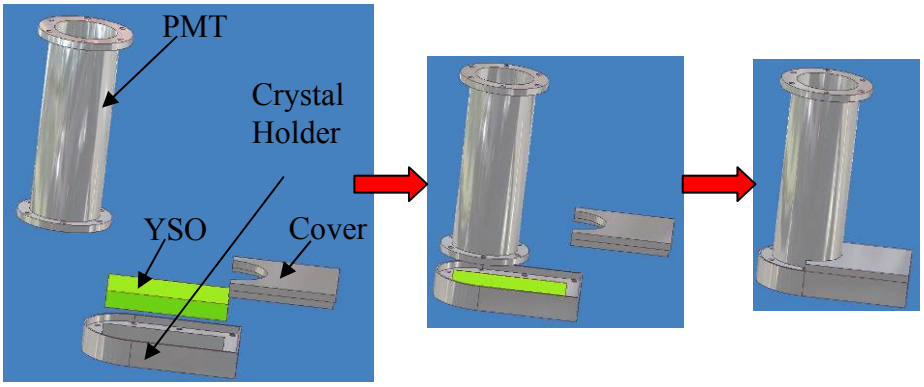

Figure 5-4. Three-dimensional rendering of the of compact system drawings for the rectangular YSO crystal holder and PMT

Rectangular versus Round Shaped YSO Crystals

Both the 2.54 cm diameter, 0.64 cm thick cylindrical, and 2.54 cm by 5.08 cm rectangular YSO crystals are optically coupled to a 2.54 cm diameter R1924A Hamamatsu PMT. Each crystal is 0.64 cm thick and surrounded by a diffuse reflector on the crystal surfaces adjacent to the crystal holder surfaces (See Figure 5-4) to increase scintillation collection efficiency. Additionally, the rectangular shaped YSO crystal has a specular reflective material on the crystal surface adjacent to the cover, because the 2.54 cm diameter PMT does not cover the entire contact surface of the rectangular crystal. Figure 5-5 is scan of the thermal protection tiles (TPS) from the belly of the space shuttle orbital with corrosion spots on the aluminum substrate just beneath the TPS tiles. The experimental setup is shown in Figure 5-2. The RSD scan was taken at 75 kVp, 8.5 mA, 1.0 mm FOC, 1.0 mm aperture, 1 mm image pixels, 0.2 s/pixels, 7 cm separation between the detector face and the surface of the TPS tiles, and 2 cm of collimation beyond the face of the detector. The results from the round and rectangular YSO detectors are shown in Figures 5-5A and 5-5B, respectively. The average counts per pixel (cpp) for the round detector is 34626 cpp and 184536 cpp for the rectangular detector. The cpp increased by 5.3 times for several reasons: The detection area of the entrance window of the rectangular detector

is 2.6 times larger than the cylindrical detector: A significant fraction of the detection area is closer to the illumination beam (higher backscatter field). Because the collimator sleeve is a fixed length, the portion of the rectangular detector closer to the illumination beam is less collimated than the cylindrical detector. The decrease is collimation is obvious with the comparison of the images in Figures 5-5A and B. Figure 5-5B appears "noisier" than Figure 5-5A because of increased signal contribution from the TPS tile (because of decreased collimation). The TPS tiles are inhomogeneous and need to be collimated out in order to increase the signal from the corrosion spots (Figure 5-5A).

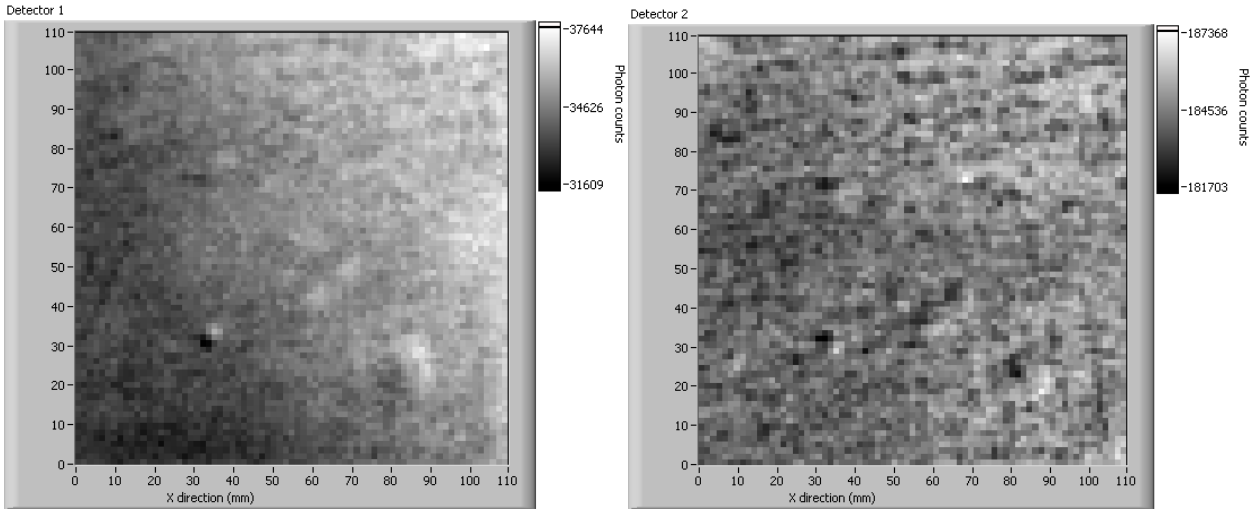

A B

Figure 5-5. Compact system RSD scan of TPS tile with corrosion on aluminum substrate with 2.54 cm diameter, A) and 2.54 cm x 5.08 cm rectangular, B) YSO crystals

Illumination Beam Evaluation

As shown in Figure 5-6, the compact illumination beam tubes are much shorter (1.9 cm and 3.8 cm) than for the Lockheed units collimators (22.9 cm). Characterization of the illumination beam is essential to predicting the performance of the compact system. The length

of the illumination beam tube and the x-ray tube electron focal spot (FOC) will have impact on the beam intensity and divergence.

Figure 5-6. Illumination beam tubes for the compact (1.9 cm and 3.8 cm) and Lockheed (22.9 cm) RSD scanning systems

Beam Intensity

The illumination beam tubes in Figure 5-6 are 22.9 cm, 3.8 cm, and 1.9 cm from top to bottom respectively. The illumination beam tubes are brass, filled with lead with an opening for the illumination beam drilled out. When the illumination beam tube is affixed to the RSD scanning system, the x-ray tube FOC is about 3.64 cm from the opening of the beam tube. An aperture is attached to the exit of the illumination beam tube as shown in Figure 5-3. The total illumination beam tube collimator length listed in Table 5-1 is the beam tube length plus the 3.64 cm offset of the FOC. The changing count rate was measured using a 2.54 cm diameter, 0.635 cm thick cylindrical YSO detector. The center of the YSO detector was 6 cm from the illumination beam, in the backscatter field, such that the detector face was positioned in the same plane as the illumination beam aperture. A 15 cm x 15 cm x 1.3 cm nylon block was located

about 6 cm from the illumination beam tube. The count rate in counts per second (cps) was measured for different illumination beam tube lengths and FOCs. The illumination aperture (1 mm), the x-ray tube HV (55 kV), the tube current (11.6 mA) and detector relative position were held constant so the only change in the measured intensity was because of the illumination beam tube length and the x-ray tube FOC.

There is a small increase in count rate when the FOC is changed from 1 mm to 3 mm as a result of an increase in solid angle between the illumination and exit aperture. As the illumination beam tube length increases the count rate continues to decrease. The count rate does not decrease as $1/R^2$, because the source is not a point source. The count rate with the 265 mm illumination beam tube is only 11.5 times lower than the count rate measured with the 55 mm tube. As shown in Table 5-1, the $1/R^2$ approximation can be used to estimate an order of magnitude change in intensity, but may be off by a factor of 2 or more. It should be noted, this is not a direct beam measurement, but a measurement of the backscatter field. Because the relative geometry of the target, detector and exit remained constant, the backscatter field intensity change is directly proportional to the illumination beam intensity change.

Table 5-1. Effect of illumination beam tube length on x-ray beam intensity with a 1 mm aperture, 55kVp, and 11.6 mA. The intensity drop does not follow a point source model (R^2)

FOC (mm)	Total Beam Collimator Length (mm)	Counts (cps)	R^2 (mm^2)	R^2 ratio	Counts Ratio*
1	55	1543234	3025	1.0	1.0
3	55	1558527	3025	1.0	1.0
1	75	1100441	5625	1.9	1.4
3	75	1116534	5625	1.9	1.4
1	265	134002	70225	23.2	11.5
3	265	135432	70225	23.2	11.5

* Ratios are calculated by dividing smaller length beam tube collimator (55 mm) count values by the larger beam tube values for the respective FOCs

Beam Dispersion

Decreasing the illumination beam tube length increases the field intensity, but at the same time increases illumination beam dispersion. In order to measure the beam dispersion, a film was placed 6 cm from the exit aperture on a lead background to reduce backscatter. An illumination spot size measurement was taken for each electron spot size (FOC) with three different length collimators. The illumination spots are shown in Figure 5-7.

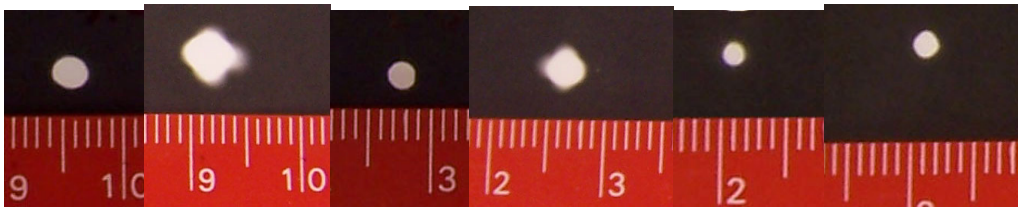

A B C D E F

Figure 5-7. Illumination spot size on film 6.0 cm from the aperture, A) 1 mm FOC, 55 cm collimator, 1.0 mAs, B) 3 mm FOC, 55 mm collimator, 1.0 mAs, C) 1 mm FOC, 75 mm collimator, 1.5 mAs, D) 3 mm FOC, 75 cm collimator, 1.5 mAs, E) 1 mm FOC, 265 cm collimator, 11.5 mAs, F) 3 mm FOC, 265 cm collimator 11.5 mAs

The x-ray tube exposure was increased for the longer illumination beam tube in order to keep the film exposure/dose (number of x-rays hitting the film) approximately constant for each of the measurements. This is essential because the film measured spot size is proportional to the film exposure. The spot size on film will continues to grow as the exposure increases because the penumbra and backscatter will artificially enlarge the illumination spot. Recall that for RSD imaging the pixel dwell time is usually adjusted so that each pixel has at least 10,000 counts to reduce statistical noise. Typically, scanning with a lower count rate (less intense illumination field) implies a longer pixel dwell time. For RSD scanning, it is typical to adjust scan time to maintain the 10,000 cpp, and therefore keep the interrogation object exposure relatively constant. In order to make a comparison between illumination spot sizes, the total exposure (mAs) was

adjusted to keep the photon fluence and film dose approximately equal, similar to how the pixel dwell time is adjusted as the count rate changes. The lowest exposure setting for the x-ray tube and controller is 1 mAs, which is adequate to saturate the film in the illumination spot. The 55 mm illumination beam tube film was exposed at 1 mAs, the 75 mm beam tube at 1.5 mAs, and the 265 mm beam tube at 11.5 mAs. These exposure times are consistent with the illumination field intensity changes measured in Table 5-1.

Figure 5-8 is an illustration of the geometric configuration that can be used to calculate the expected maximum divergence of the illumination beam penumbra. Given the geometry shown in Figure 5-8, the illumination spot size can be easily calculated by S = (A/F)(D+F), where F=A/(A+FOC)*(L). Each of the variables is defined as:

- FOC – electron focal spot diameter on x-tube anode target
- F – optical focus location with respect to the illumination beam aperture and illumination spot
- D – separation distance between the aperture exit and position where the illumination spot size is measured
- L – length of the illumination beam collimator from the x-ray tube FOC to the exit beam aperture
- S – illumination spot diameter at a distance (D) from the exit aperture
- A – diameter of the illumination beam exit aperture

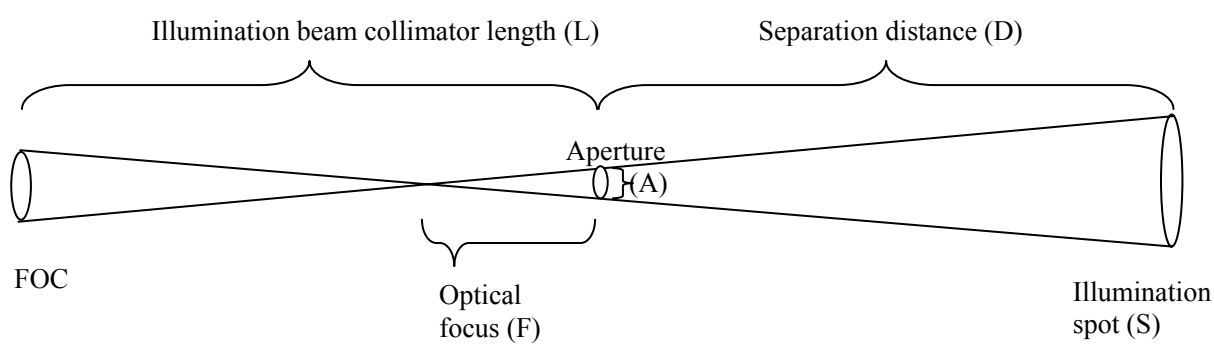

Figure 5-8. Geometric configuration to calculate illumination beam spot divergence

Table 5-2 is a summary of calculated and measured illumination beam spot sizes. Some of the spots sizes for the 3 mm FOC show a large penumbra, Figure 5-7B and D, indicating non-uniformity in the electron spot on the tungsten target in the x-ray tube. The large penumbra is not only because of the larger FOC diameter, but partially related to the short exposure of 1 mAs. The short exposure does not allow the FOC to fully develop as HV is ramped up and down again.

Table 5-2. Calculated versus measured illumination spot sizes for different length illumination beam tubes and focal spot sizes

FOC (mm)	Beam Collimator Length (mm)	Aperture (mm)	Film Distance (mm)	Calculated (mm)	Measured (mm)	(mm)	Exposure (mAs)
1	55	1	60	3.2	3.0	+/- 0.25	1.0
3	55	1	60	5.4	5.0	+/- 1.0	1.0
1	75	1	60	2.6	2.5	+/- 0.25	1.5
3	75	1	60	4.2	4.0	+/- 1.0	1.5
1	265	1	60	1.5	1.5	+/- 0.25	11.5
3	265	1	60	1.9	2.0	+/- 0.25	11.5
5.5*	270	1	60	2.4	2.5	+/- 0.25	11.5

* Measure on 160 kVp Lockheed system

To further analyze the illumination spot size diameter, each film was digitized using flatbed scanner with 8 bit grayscale. A horizontal-line profile across the center of the illumination beam was generated using MATLAB. Figure 5-9 shows the illumination beam spots for the 1 mm and 3 mm FOCs with illumination beam tube lengths of 55 mm, 75 mm and 265 mm. Because the 75 mm illumination beam tube collimator with a 1 mm FOC is typically used with the compact RSD scanning system, it is compared to the longer illumination beam tube collimator used in the Lockheed RSD scanning systems in Figure 5-10. The horizontal-line profile for 1 mm FOC with the 75 mm illumination beam collimator closely matches the profile obtained with the 3 mm FOC, and the 265 mm long illumination beam collimator. Based on having nearly identical beam dispersion measurements at 6 cm from the illumination spot, and

having a count rate 11.5 times higher than the longer 265 mm illumination beam collimator at the same current, the compact RSD scanning system has been able to obtain the same resolution and quality image faster than the previous generation scanners. It should be noted that while the 75 mm beam tube with the 1 mm FOC compares well with the 3 mm FOC, 265 mm illumination beam tube, the larger FOC can run at a higher current, increasing the beam intensity. The longer illumination beam tube suffers less divergence as a function of depth. Illumination beam collimator length, aperture and x-ray FOC are selected based on application requirements balancing beam spot and scanning speed.

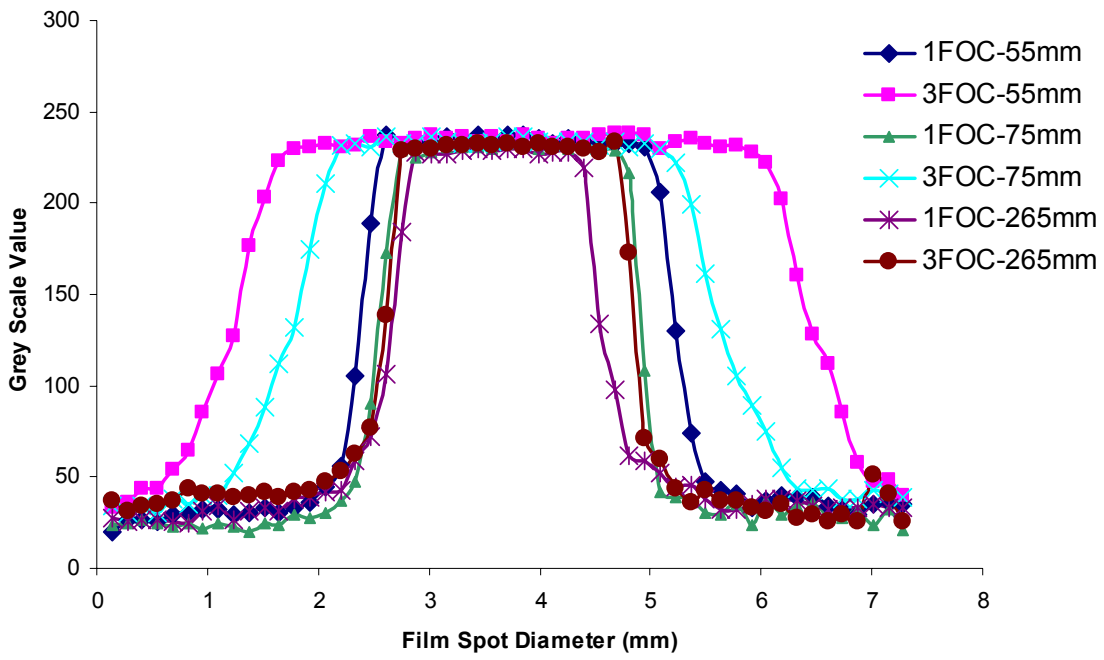

Figure 5-9. Horizontal line profile of illumination beam spot size for various x-ray focal spots (FOC) and illumination beam tube collimator lengths of 55mm, 75 mm and 265 mm

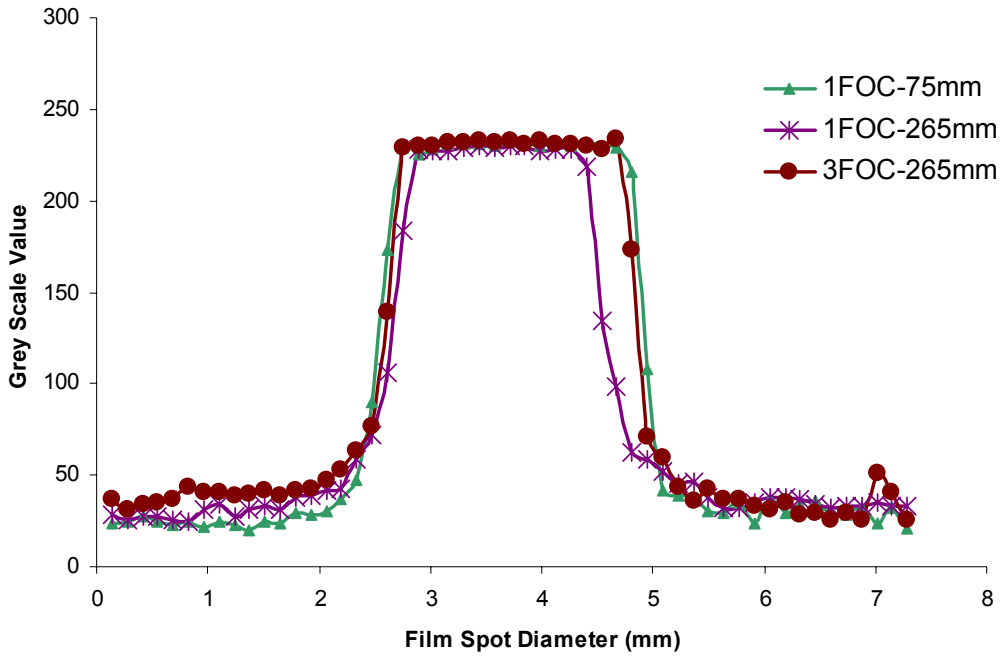

Figure 5-10. Horizontal line profile of illumination beam spot size for various x-ray focal spots (FOC) comparing 75 mm to the 265 mm illumination beam tube collimator

CHAPTER 6
SNAPSHOT BACKSCATTER RADIOGRAPHY

Image Technology Introduction

"Detector" is used in the general sense of any media capable of rendering film-like x-ray images. Computed radiography (CR) plates consist of a film-like plate with a phosphor coating. Electrons are excited to metastable state, and essentially store the image until they are read by a CR reader (ACR). The ACR scans the CR plate with an intense red laser, and measures the output light released from the electron transition to a ground state with PMTs. CR plates have the advantage of being flexible with handling procedures similar to film. Digital radiography (DR) utilizes detectors (typically solid state or scintillator) that may be coupled to complementary metal-oxide semiconductors (CMOS) arrays and associated electronics for digitizing the radiographic images real-time. DR typically consist of a plate-like structure, that is not flexible and significantly thicker than CR plates. DR plates are on the order of centimeters thick with resolution limits currently around 100-150 microns, but offer the ability to take real-time motion images. Any detector capable of rendering film-like x-ray images may be used.

Snapshot Backscatter Radiography (SBR)

The idea of snapshot backscatter radiography is to generate a backscatter image without scanning. The detector would be placed over the object that is going to be imaged (Figure 6-1). The exposure would be taken directly through the detector, and the backscatter image could be captured. Knowing the first-pass exposure, it could then be digitally subtracted from the image leaving only the backscatter image.

This first series of experiments were conducted using lead letters on a nylon surface (Figure 6-1A). A single x-ray exposure was then taken using a photostimuable phosphor-based image plate or CR plate (Kodak GP Digital Imaging Plate SO-170 with a VMI ACR reader)

(Figure 6-1B). The x-ray generator focus (FOC) was positioned about 58.4 cm above the CR plate. A sample of a raw unprocessed image taken at 50 kVp, with a 2.85 mAs exposure is shown in Figure 6-2. The striping down the center of the image is caused by the film cover sleeve (Figure 6-1B).

A 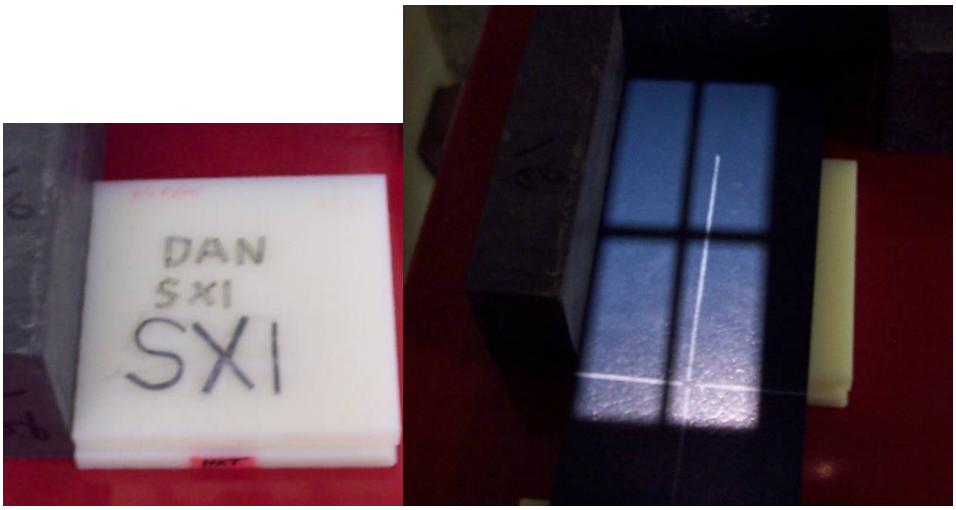

B

Figure 6-1. Snapshot backscatter radiography setup, A) lead letters on nylon, B) single exposure x-ray being taken through digital film

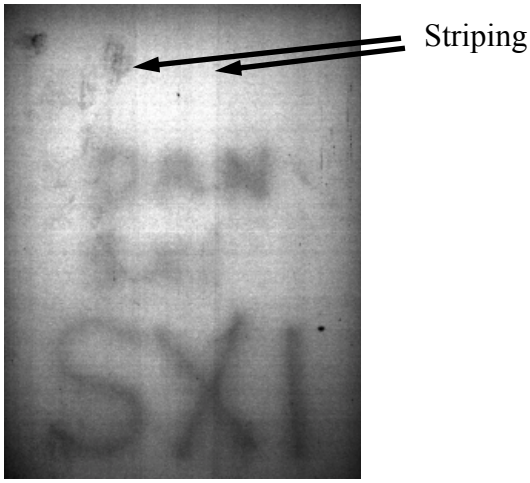

Figure 6-2. Unprocessed snapshot backscatter image

While an image is present in Figure 6-2, the first-pass of illumination x-rays through the CR plate creates a strong signal onto which the backscatter signal is superimposed. While the backscatter signal could be somewhat enhanced with image processing, knowing the first-past distribution, the SNR would still need to be increased to create higher resolution images with more contrast. Shadow aperture backscatter radiography increases the SNR.

Shadow Aperture Backscatter Radiography (SABR)

The concept of shadow aperture backscatter radiography (SABR) is illustrated in Figure 6-3. The entire field is illuminated, similar to SBR, except an aperture is present to shape the illumination field. The aperture allows the illumination field to penetrate the interrogation object and scatter. The backscatter components then generate an image on the portion of the detector that is shadowed from the illumination field.

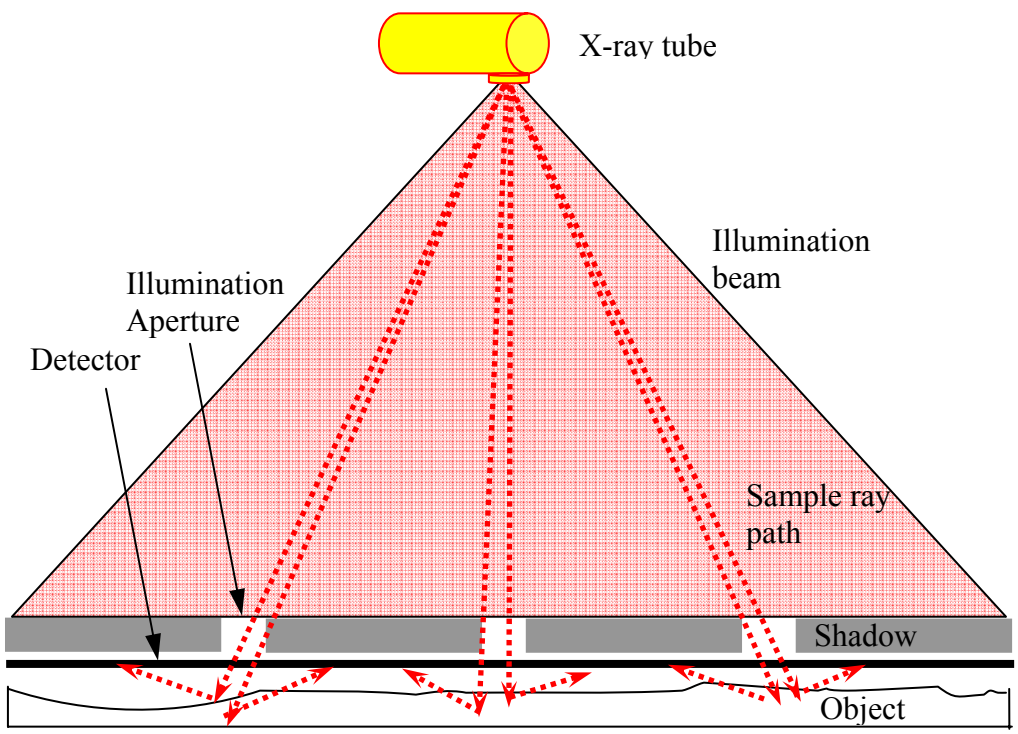

Figure 6-3. Shadow aperture backscatter radiography illustration

The SABR method of SBR more efficiently uses the dynamic range of the detector. The backscatter signal is no longer superimposed on the illumination transmission signal. The illumination field shaping shadow aperture does not have to be in direct contact with the detector, but may be positioned anywhere in the illumination beam.

SABR Nylon Substrate Measurements

The x-ray source is a Source Ray SR 115 portable veterinarian x-ray generator that varies in voltage from 30 to 115 kV. The maximum single shot exposure is 60 mAs with about a two minute cooling and recharging cycle between shots. The object was placed on a steel table, the CR was placed over the object and the shadow aperture was positioned over the CR. The shadow apertures were cut from 1.06 mm thick sheets of lead. Figure 6-4A shows a shadow aperture which consists of a combination of lead squares and lead strips. The squares vary in size from 0.635 cm to 5.08 cm in 0.635 cm increments (0.25 inch to 2 inch in 0.25 increments). The long rectangular lead strips are about 3 cm in width. The shadow aperture illumination separation spacing is about 1 mm or less. Figure 6-4B is an example of a uniform shadow aperture.

Figure 6-4. Shadow aperture examples with A) various size lead shadows B) Uniform shadow aperture grid pattern

Figure 6-5 is a collection of various brass, aluminum and steel washers, nuts, and lead pieces (i.e. foreign object debris (FOD)) on a 6/6 nylon substrate. Integrated exposure in mAs was incremented up in 10 mAs steps until the image on the CR plate reaches an adequate level of exposure in the shadow backscatter region. The amount of exposure required depends on several factors: aperture grid spacing, the size of the shadow area, the kV of the x-ray tube, the illumination object's scatter-to-absorption ratio and the mean-free-path (mfp) of scattered photons in the object. Increasing the illumination aperture spacing, kV, scattering-to-absorption ratio and mfp have a tendency to reduce the required exposure

Figures 6-6 and 6-7 are SABR images of the target (Figure 6-5). The exposures were taken at 70 kVp, 120 mAs, and 120 cm from the x-ray tube FOC. Each of SABR images shows most of the FOD. Figure 6-6 shows the results from a 2.54 cm square uniform shadow aperture configuration. Figure 6-7 is a SABR image using a shadow aperture with a variety of different geometries tested simultaneously. Figures 6-8 and 6-9 are line profiles for column 767 and row 917, respectively.

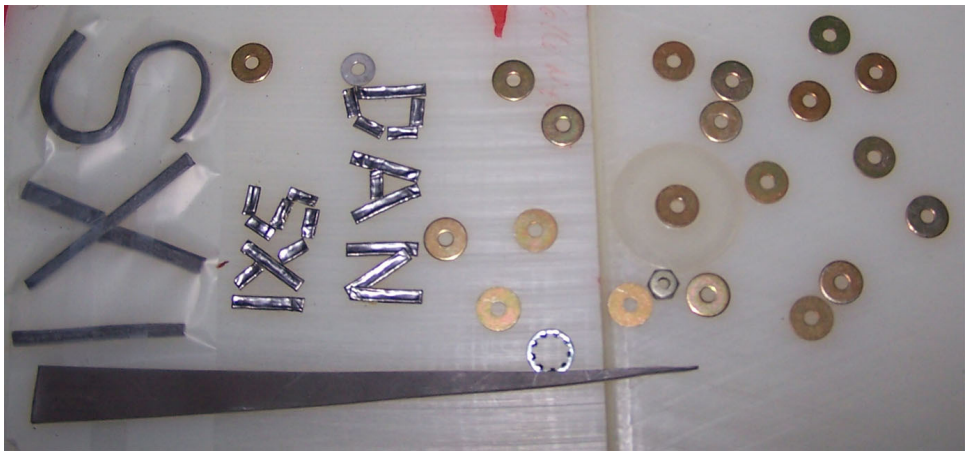

Figure 6-5. Collection of washers and lead on a nylon substrate

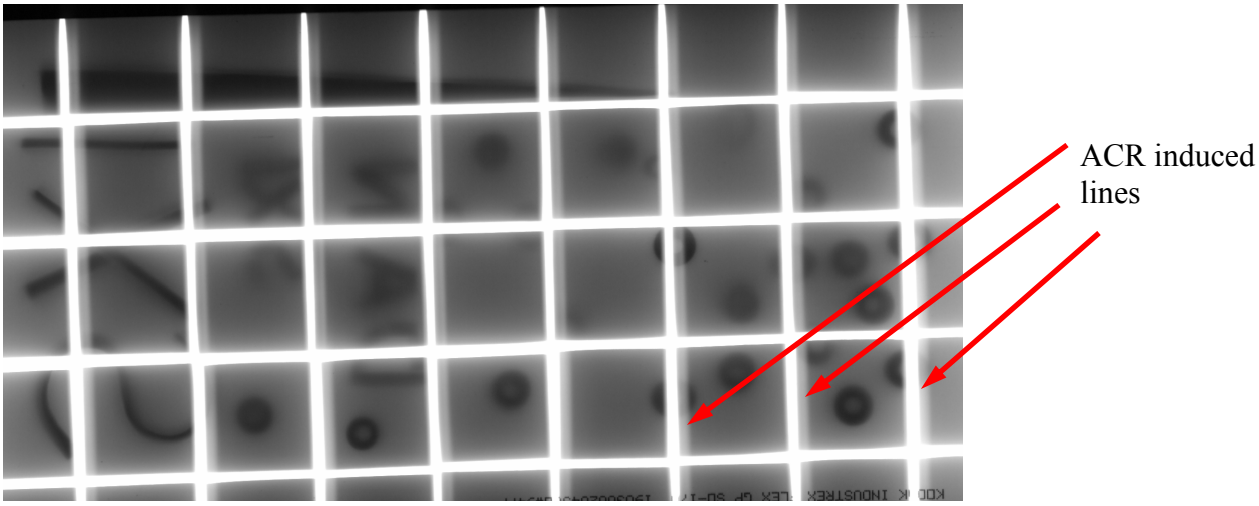

Figure 6-6. SABR image of Figure 6-5 target using 2.54 cm square shadow aperture, 70 kVp, 120 mAs, 120 cm from x-ray FOC.

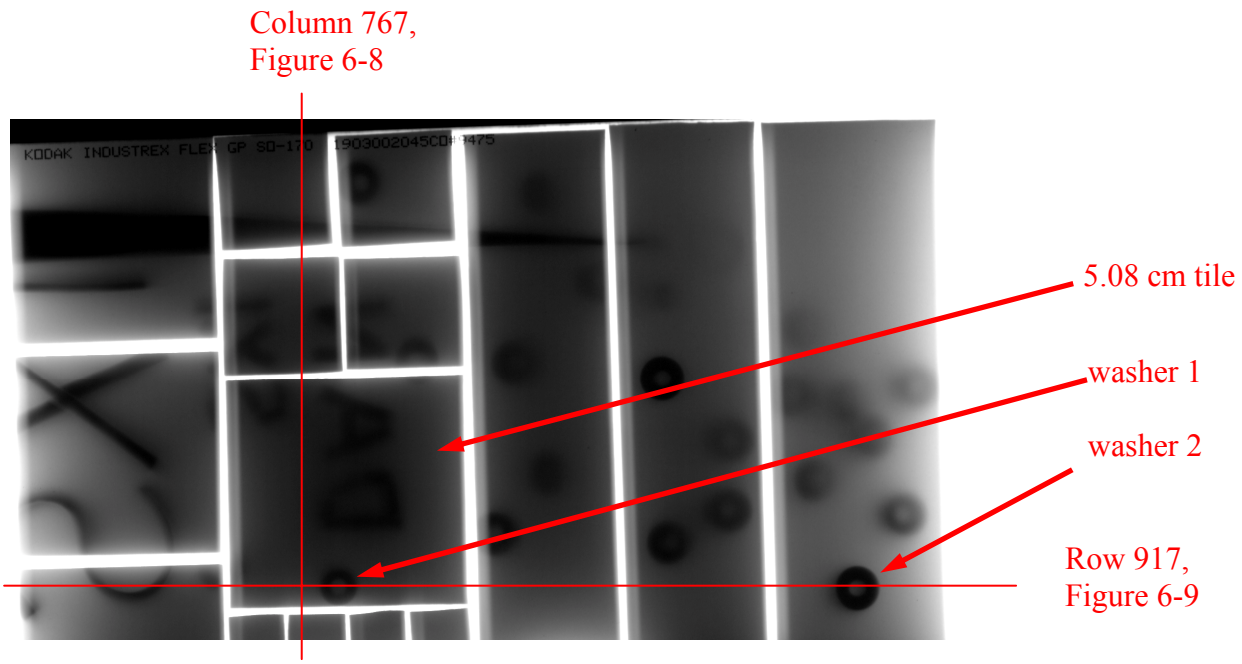

Figure 6-7. SABR image of Figure 6-5 target using various dimension shadow apertures, 70 kVp, 120 mAs, 120 cm from x-ray FOC

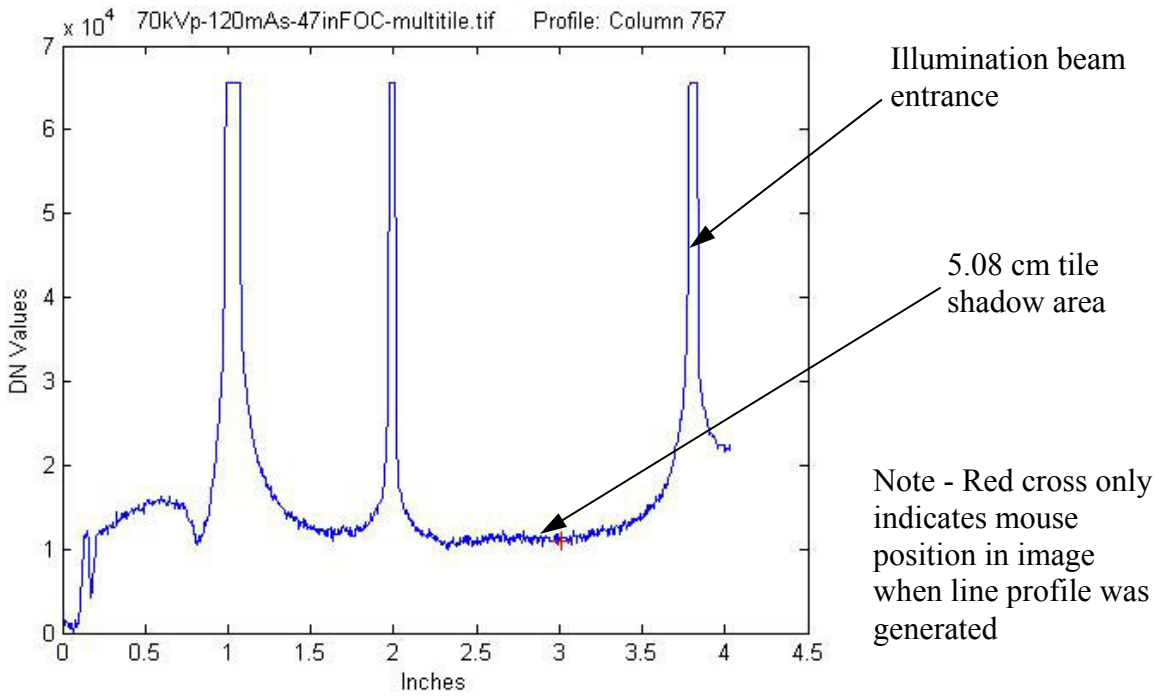

Figure 6-8. Line profile of column 767 shown in Figure 6-7. The right side of the image corresponds to the bottom of the line profile shown in Figure 6-7.

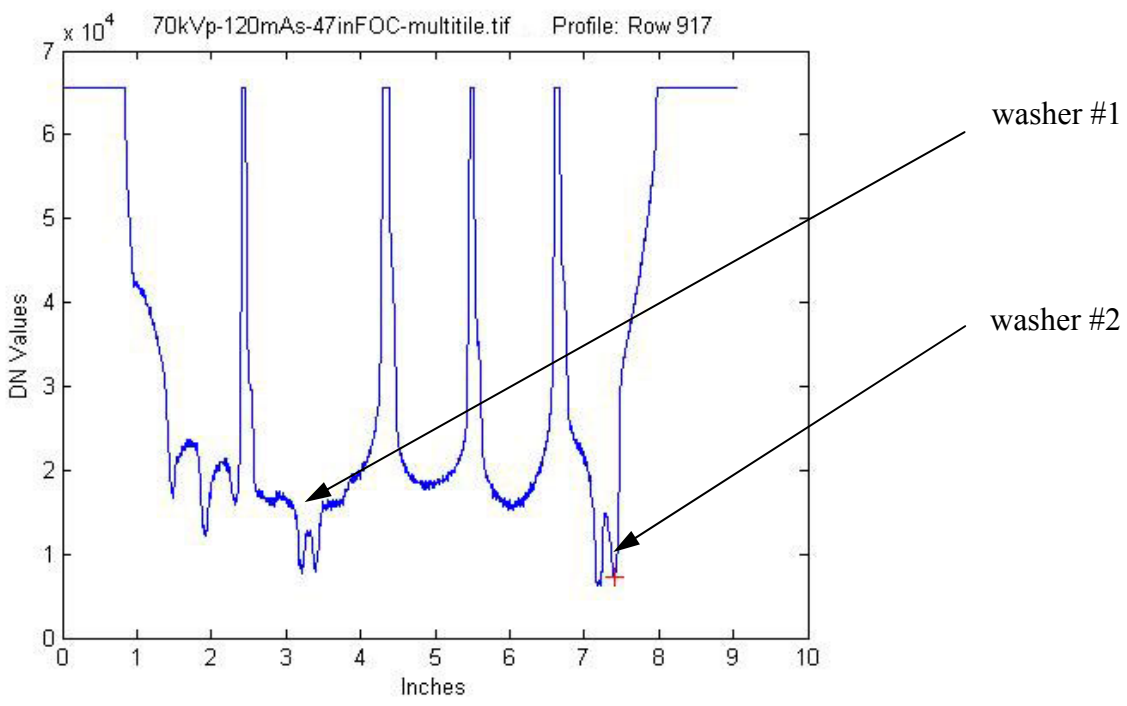

Figure 6-9. Line profile of row 917 shown in Figure 6-7

SABR Nylon Substrate Discussion

Figure 6-6 is a SABR image using a 2.54 cm uniform square shadow aperture grid with 1 mm illumination apertures. While most of the FOD is visible, the relative FOD contrast compared to Figure 6-7 is discernably lower for many articles. For many of the FOD objects, the relative position with respect to the shadow aperture plays a significant role in the relative contrast. For example, washer #1 has a relative contrast of about -53 % in both figures; however, washer #2 has a relative contrast of -62 % in Figure 6-6 and -73% in Figure 6-7.

In Figures 6-6 and 6-7 there is a bright region just to the right of the illumination area. These bright regions in the shadow area are induced by the CR reader (ACR). The CR plates are fed into the ACR and read from left to right as shown in the image. The saturated illumination areas leave an afterglow in the reading process.

Additional insight into the SABR process is available in the line profiles of the images. Figure 6-8 is a line profile across column 767of Figure 6-7. Moving from left to right in the figure, the scatter intensity starts very low. Just before the CR is completely saturated around 2.54 cm (1 in) there is a decrease in signal induced by the wedge-shaped piece of lead. From the saturation peak, the backscatter signal drops off first as a step function at the shadow aperture edge, then with an exponential profile in the shadow region. A second saturation peak is located at 5.08 cm (2 inches). The area between the two saturation peaks is a superposition of two decaying exponentials. When the distance and size of the illumination aperture and shadow regions approach an optimal setting, the two decaying exponentials give way to a region where the scatter signal is relatively flat. This large plateau region as shown between 5.08 cm (2 inches) and 10.16 cm (4 inches) is the area where the dynamic range of the film can be utilized to generate a SABR image without any image processing. The average mfp for a 70 kVp x-ray spectrum based on MCNP simulations for nylon 6/6 is about 5.5 cm, indicating that optimal

shadow aperture spacing for a nylon substrate may be around 1 mfp. It is important to remember this estimate is determined using a homogeneous substrate, with FOD located only on the surface, nearly in contact with the CR plate. Any type of structure or inhomogeneities is expected to change the optimal shadow aperture pattern. Figure 6-9 is a line profile of Figure 6-7 taken from row 917. The backscatter signal response in the shadow regions induced by washer #1and #2 start at 7.62 cm (3 inches) and 17.8 cm (7 inches), respectively.

SABR Aluminum Substrate Measurements

Nylon is nearly an ideal substrate for backscatter experiments in contrast to aluminum. For example, at 35 keV the scatter-to-absorption ration of nylon is 5.1 and aluminum is 0.3. Figure 6-10 is an aluminum substrate consisting of two pieces of aluminum. The aluminum plates are about 15.2 cm x 15.2 cm x 1.27 cm. The FOD consists of brass, steel, aluminum and nylon washers along with a few pieces of lead. Figure 6-11 is the resulting SABR image using the shadow aperture from Figure 6-4(A). The exposure was taken at 75 kVp, 240 mAs, and 120 cm from the x-ray tube FOC.

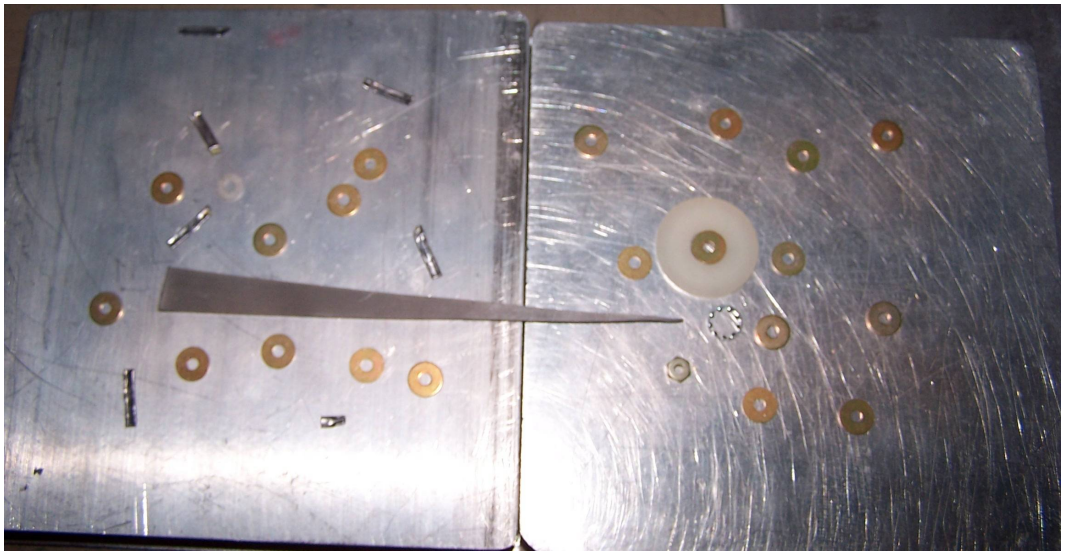

Figure 6-10. Collection of washers and lead on an aluminum substrate

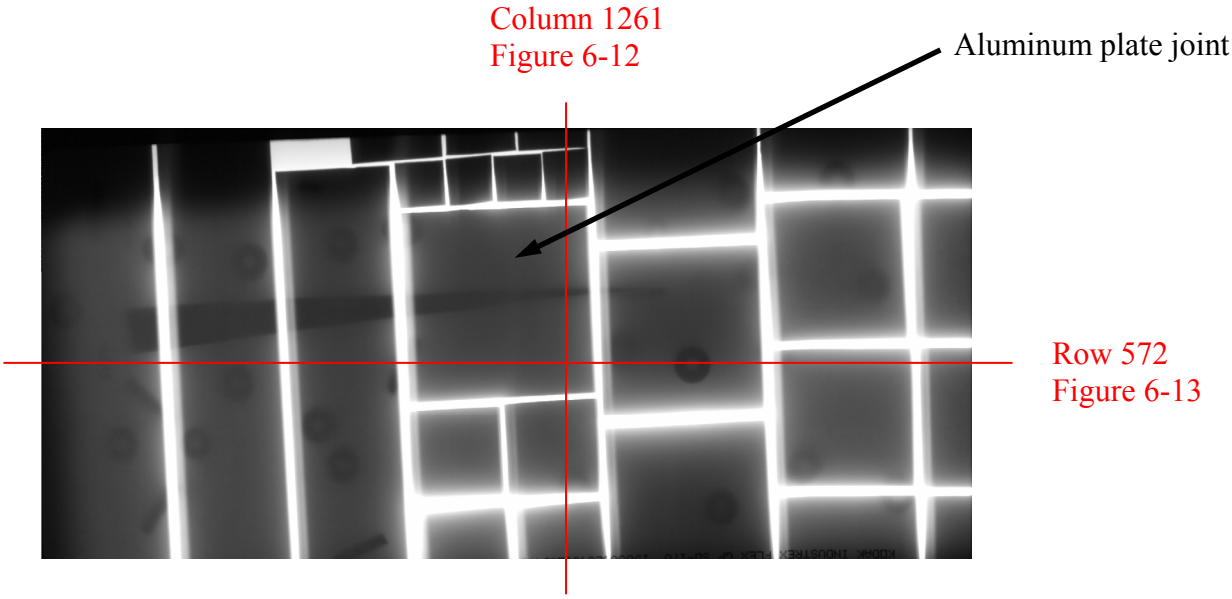

Figure 6-11. SABR image of FOD on aluminum substrate target (Figure 6-10) using various dimension shadow apertures, 75 kVp, 240 mAs, 120 cm from x-ray FOC

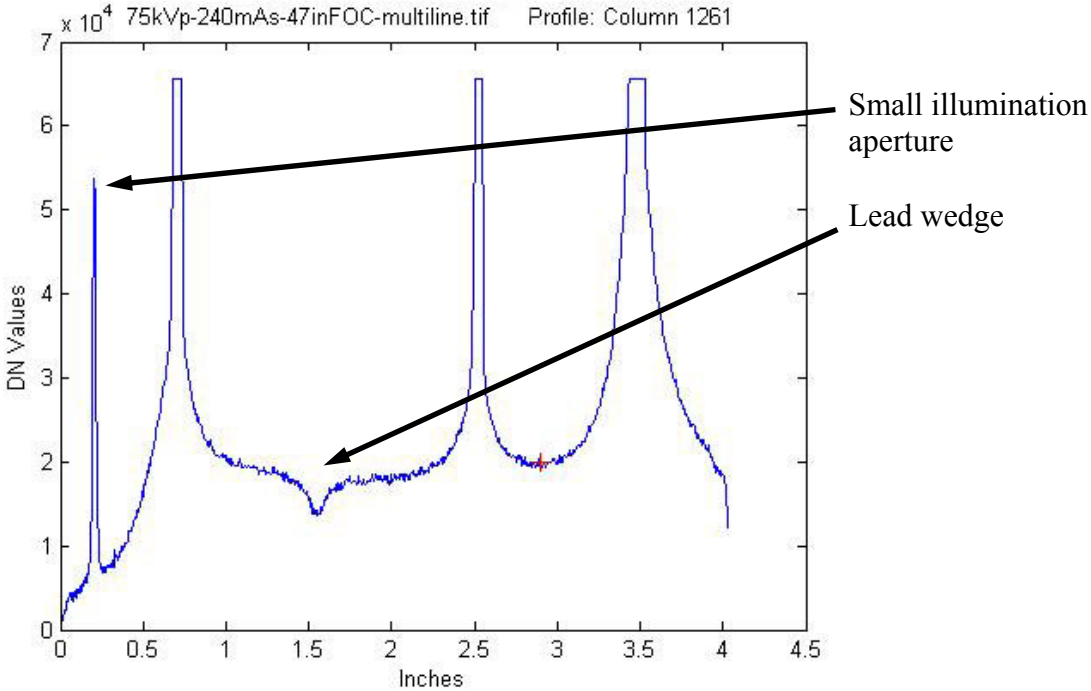

Figure 6-12. Line profile of column 1261 shown in Figure 6-11. The right side of the figure corresponds to the bottom of line profile shown in Figure 6-11.

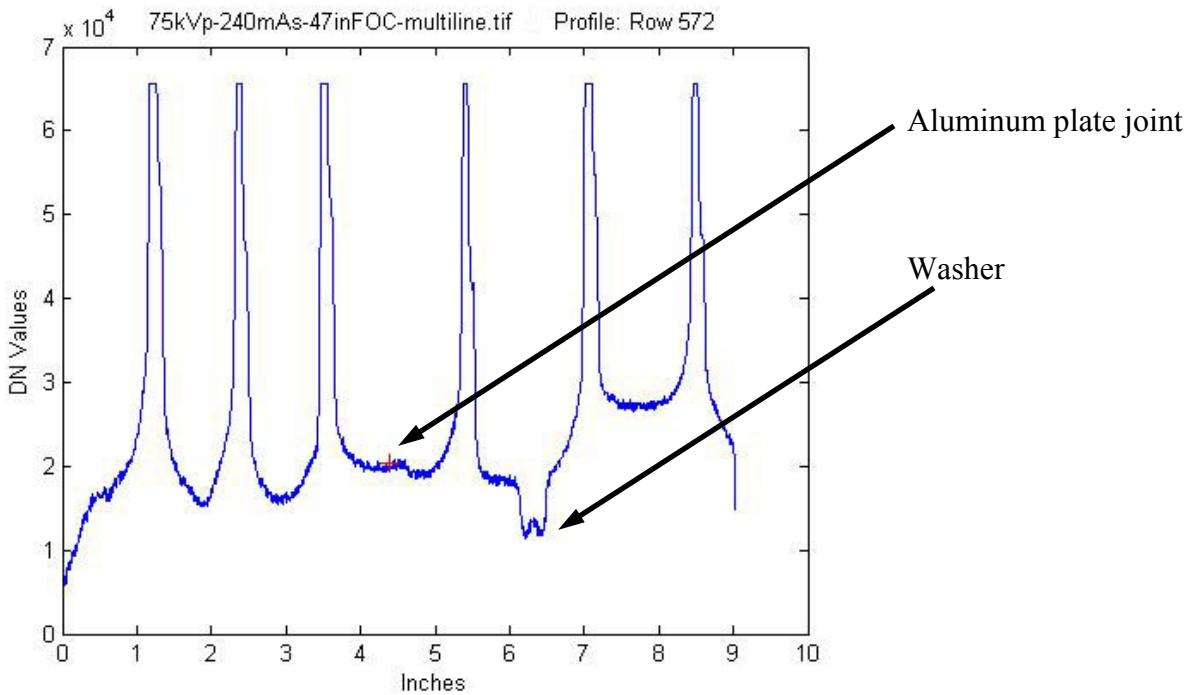

Figure 6-13. Line profile of row 572 shown in Figure 6-11.

SABR Aluminum Substrate Discussion

Figure 6-11 is a SABR image using a multi-dimensional square shadow aperture grid with most illumination apertures being about1 mm. A line profile of column 1261, Figure 6-12, demonstrates the effect of making the illumination aperture too small. The apertures is nearly closed, ~0.25 mm, (Figure 6-11) and as a result, the illumination intensity does not saturate during the 240 mAs exposure.

Figure 6-13 is a line profile of row 572 in Figure 6-11. Visible in both the SABR image and line profile is the joint of the aluminum plate. The ability of SABR to locate the joint position indicates this technique may be suitable for imaging cracks.

In Figure 6-6 and 6-7 there is a bright region just to the right of the illumination area. These bright regions in the shadow area are induced by the CR reader (ACR). The CR plates are

feed into the ACR and read from left to right as shown in the image. The saturated illumination areas leave an afterglow in the reading process.

SBR Radiography Lessons Learned and Failed Attempts

The first SBR images suffered from having a small backscatter signal superimposed on a large illumination signal (Figure 6-2). Using a mask pattern with 6.35 mm apertures on a 6.35 mm x-y pitch (Figure 6-14A) was the first attempt to generate a SABR image. Rectangular illumination apertures were chosen to keep the backscatter field in the shadow region as uniform as possible. However the shadow-to-illumination area ratio was not favorable (Figure 6-15A). Even with the contrast adjustment, the falling step function followed by the rapidly decaying exponential change dominates the signal.

Figure 6-14B is an attempt to adjust the shadow-to-illumination area ratio to a more favorable condition. The pattern uses 1 mm circular illumination apertures on a 6.35 mm x-y pitch. The horizontal striping pattern of increased intensity that is not present in the vertical direction is due to the ACR. However the decaying exponential signal around the aperture holes yields only a small annular region where the SABR image can be easily registered without image processing as seen in Figure 6-15B and illustrated in Figure 6-16.

The progression of experiments led to the development of the square and long rectangular shadow aperture designs. The long rectangular shadow aperture patterns shown on left side of Figure 6-4A creates a large shadow areas, where the backscatter field is relatively uniform. The illumination and shadow pattern generated with long rectangular shadow apertures is illustrated in Figure 6-17. Items such as FOD and cracks can then induce a backscatter signal change that registers as an image without requiring significant image processing.

A 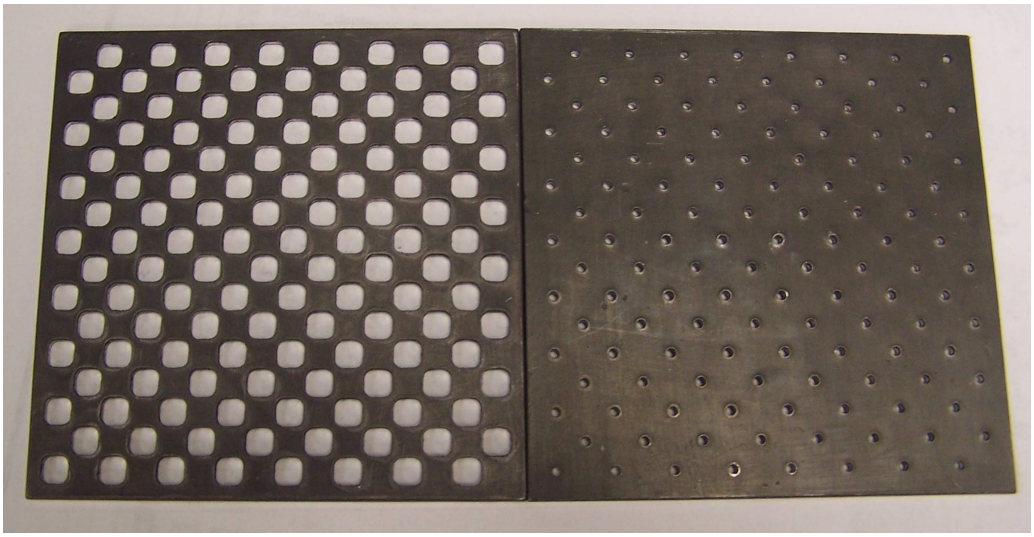 B

Figure 6-14. SBR mask patterns, A) large 6.35 mm aperture, B) small 1 mm aperture

A 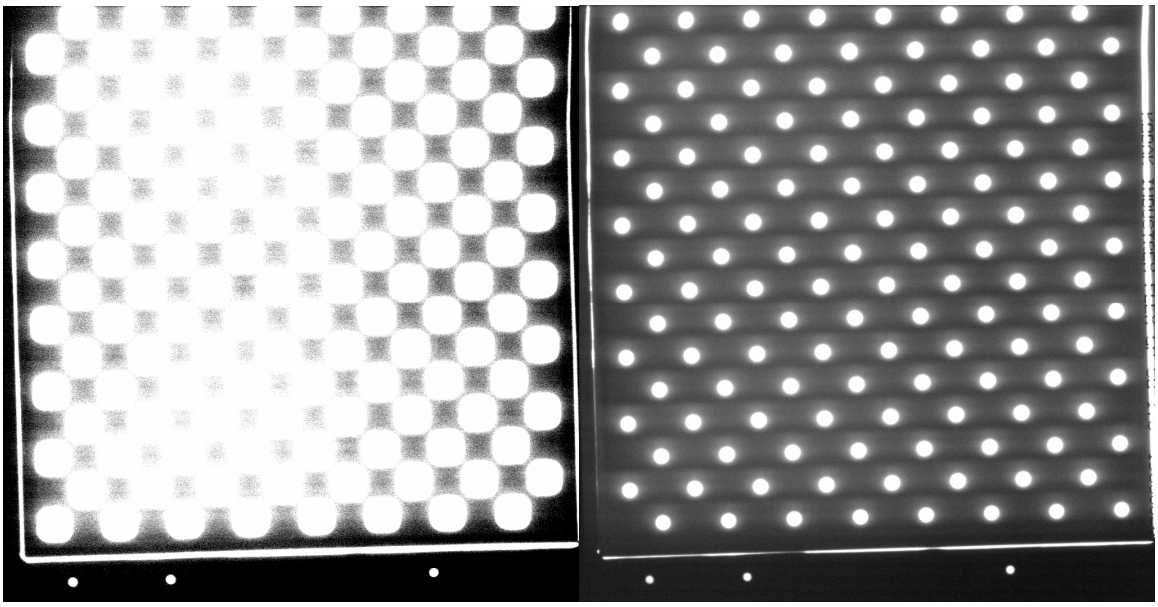 B

Figure 6-15. SBR exposures taken at 70 kVp, 30 mAs, 120 cm from FOC, A) Large 6.35 mm SBR image B) 1 mm small aperture SBR image.

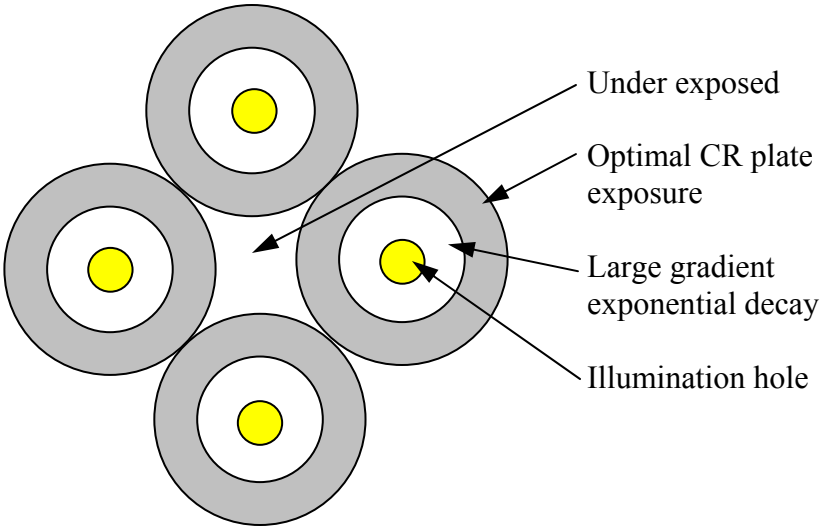

Figure 6-16. SABR exposure pattern for round illumination apertures

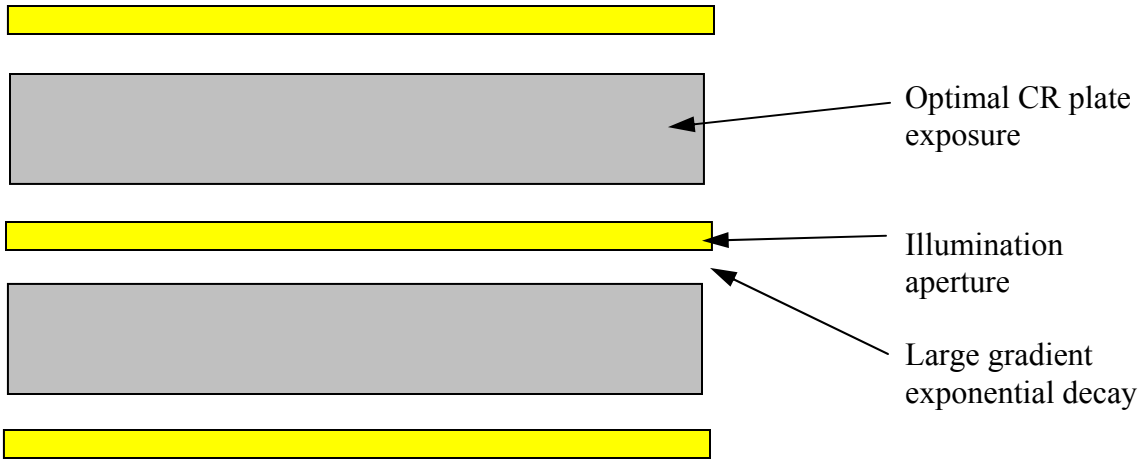

Figure 6-17. SABR exposure pattern for line illumination apertures

CHAPTER 7
SUMMARY, CONCLUSIONS AND FUTURE WORK

Summary and Conclusions

Radiography by selective detection (RSD) is a pencil beam Compton backscatter imaging technique developed at the University of Florida that falls between highly collimated and uncollimated techniques. RSD is orders of magnitude faster than highly collimated techniques, but offers depth resolution that is not available in uncollimated CBI techniques. In addition to depth resolution, RSD allows for preferential detection of backscatter components that are responsible for improving image contrast.

Lateral Migration Radiography (LMR) is a subset of RSD where the image contrast is dominated by third order (and higher) scatter x-ray components that was used for landmine detection. Because typically the illumination x-ray beam penetration barely extends to a depth much beyond the base of the mine, the mine (or surrounding soil) becomes a diverged scattered x-ray source for the highly collimated detectors. While second order scatter components are still close to the penetrating beam, third and higher order scatter components scatter far enough from the original beam, to produce a laterally-spread scatter source in the landmine (or surrounding soil). Typically, very large detectors (on the order of 0.3 m^2) are required to capture these laterally-spread, multiple-scatter components

RSD scanning systems are currently being used by Lockheed Martin Space Systems Co. and NASA for inspection of the spray-on-foam-insulation on the space shuttle external tank. For these systems current mode detector operation was found to significantly increase the contrast of deep void defects in SOFI without adversely affecting the contrast of shallow void defects. Optimization and analysis of the illumination beam tube and detector components of the Lockheed RSD scanning systems has led to the development of a compact scanning system. The

compact scanning system uses YSO detectors in place of NaI detectors. YSO is not only faster than NaI, with more light output, but it is not hydroscopic and more rugged. Overall the new compact scanning systems are about 60 % lighter and 60 % smaller by volume than the original systems, yet have the ability to maintain and/or exceed resolution and scanning speed of the previous generation of scanners.

A new technique of Snapshot Backscatter Radiography (SBR) has been developed. Shadow Aperture Backscatter Radiography (SABR) uses a collection of shadow and illumination areas designed to generate single exposure backscatter images. The SABR technique more efficiently utilizes the dynamic range of the imaging media (film, detector, CR, DR, etc.) by limiting the illumination area, and generating the backscatter image on the shadow regions of the imaging media. While further optimization of the technique is required, SABR has from a proof-of-principle stage of development to an experimental laboratory procedure.

SXI (RSD, LMR, or SABR) is a single-sided imaging technique in which the radiation source and the detection/imaging device are located on the same side of the object. SXI is a valuable non-destructive evaluation (NDE) tool because of its single-sided nature, penetrating abilities of radiation, and unique interaction properties of radiation with matter. This technology can be applied in many fields including NDE, medical, security, and military applications.

Future Work

The most significant drawback of RSD imaging is still image acquisition time. Although the compact system shortened illumination beam tube may increase scanning speed by a factor of three, (beam intensity increases by a factor of 11.2, but x-ray tube current limit decreases by a factor of 3.86 using a smaller focal spot to maintain resolution, leaving a net gain of only about three) innovative ways of improving image acquisition time are needed. Exploration of illumination beam and detector relative geometry could hold many of answers. An example

would be the use of multiple illumination beams, each surrounded with an array of detectors. New image processing algorithms should be tested; it could be possible to tolerate increased statistical noise (lower pixel dwell time), if a post processing filter algorithm removes the noise.

The RSD imaging processing software needs further research. The majority of RSD images are in raw data format. The limited amount of image processing, such as combining different detector images through addition and subtraction, has shown significant potential. The landmine application is the perfect example. Also, there is significant embedded information in each of the detector images that needs to be properly correlated to enhance the image. It may even be possible to generate 3-D images with the use of an array of angled detectors, similar to laminography techniques.

Current mode detector operation has been found to enhance the contrast of deep voids in SOFI using NaI detectors. This is because the spectrum hardens with depth of penetration and current mode weights the image contrast by energy and intensity. Because of the importance of energy to deeper feature contrast, this phenomenon should be explored for other types of defects in various materials using other detectors such as YSO. It would be very useful to acquire the pulse height spectrum during image acquisition, pixel by pixel. In current mode, the energy weighting is fixed, but with the acquired spectrum, pixel contrast can then be weighted by energy allowing the user to define or vary the importance of different energy groups. The use of energy weighting as a type of collimation should be further explored.

Shadow Aperture Backscatter Radiography used 1/24 inch thick lead for the shadow aperture. This limits the x-ray energy to about 70 kVp before the transmission signal (through the lead) begins to significantly reduce the SNR. Thicker lead or other materials such as tungsten should be explored for this application allowing for experimentation with higher

energy. Filtering the illumination field hardens and narrows the spectrum which may reduce image distortion and blurring, because as the spectrum hardens and narrows, there should be less variance in the mfp of the scattered photons. A different x-ray source other than the SR-115 should be used because it is only capable of 60 mAs exposures and the typical exposure for SABR with an aluminum substrate is about 240 mAs.

LIST OF REFERENCES

1. E. Odeblad and A. Norhagen, " Electron Density in a Localized Volume by Compton Scattering", *Acta Radiologica*, **45** p. 161-167 (1956)

2. M.A. Kumakhov, A.F. Gamaliy, V.N. Vasiliev, M.Yu. Zaytsev, K.V. Zaytseva "Scattered X-rays in medical diagnostics", Proceedings of SPIE, **59** p. 43 (2005)

3. M. Annis, M. Johnson, and R. Mastronardi, "Tomographic imaging with concentric conical collimators", *United State Patent,* 4,825,454 (1989)

4. S. Anghaie, L. Humphries, and N. Diaz, "Material characterization and flaw detection, sizing, and location by the differential gamma scattering spectroscopy technique. Part I: development of theoretical basis.", *Non-Destructive Testing and Evaluation International*, **28**(3) p. 192 (1995)

5. S. Anghaie, L. Humphries, and N. Diaz, "Material characterization and flaw detection, sizing, and location by the differential gamma scattering spectroscopy technique. Part II: experiment", *Non-Destructive Testing and Evaluation International*, **28(**3) p. 192 (1995)

6. A.D. Dougan, "http://www.llnl.gov/sensor_technology/STR21.html", Lawrence Livermore National Lab (LLNL) (1995)

7. S. Anghaie, "Accuracy improvement for gamma-ray techniques in two-phase measurements", Ph.D. Thesis, The Pennsylvania State University (1982)

8. E.S. Kenny, and A.M. Jacobs, "Dynamic Radiography", *United States Patent*, 3,769,507 (1973)

9. S.H. Nellis, A.J. Liedtke, M.L. Heimer, R.A. Shiroff, A.M. Jacobs et al.,"Validation of dynamic radiography in the dog and evaluation of ischemic dyssynergy", *The American journal of physiology*, **238**(1) p. 43-53 (1980)

10. R. H. Bossi; J. L. Cline; K.D. Fridell; J.M. Nelson, "One sided radiographic inspection using backscatter imaging", *Non-Destructive Testing and Evaluation International*, **28**(3) p.192 (1995)

11. W.J. Baukus, "X-ray imaging for on-the-body contraband detection" Proceedings of SPIE, **2932** p. 115-120 (2000)

12. A. Jacobs, and J. Campbell, "Landmine detection by scatter radiation radiography," Scientific and Technical Final Report, Contract DAAK 70-86-K-0016, U.S. Army Belvoir Research, Development and Engineering Center, (1987)

13. J. Campbell, and A. Jacobs, "Detection of buried land mines by Compton backscatter imaging," *Nuclear Science and Engineering*, **110** p. 417-424 (1992)

14. Y. Watanabe, J. Monroe., S. Keshavmurthy, A. Jacobs, and E. Dugan, “computational methods for shape restoration of buried objects in Compton backscatter imaging”, *Nuclear Science and Engineering*, **122** p. 55-67 (1996)

15. J. Wehlburg, S. Keshavmurthy, E. Dugan, and A. Jacobs, “Geometric considerations relating to lateral migration backscatter radiography (LMBR) as applied to the detection of landmines," Proceeding of SPIE, **3079** p. 384-393 (1997)

16. Z. Su, J. Howley, J. Jacobs, E. Dugan, and A. Jacobs., “The discernibility of landmines using lateral migration radiography”, Proceeding of SPIE, **3392** p. 878-887 (1998)

17. C. Wells, Z. Su, J. Moore, E. Dugan and A. Jacobs, "Lateral migration radiography measured image signatures for the detection and identification of buried landmines”, Proceeding of SPIE, **3710** p. 906-916 (1999)

18. C. Wells, Z. Su, A. Allard, S. Salazar, E. Dugan and A. Jacobs, “Suitability of simulated landmines for detection measurements using x-ray lateral migration radiography”, Proceeding of SPIE, **4038** p. 578-589 (2000)

19. Z. Su, A. Jacobs, E. Dugan, J. Howley, and J. Jacobs, “Lateral migration radiography application to land mine detection, confirmation and classification,” *Optical Engineering*, **39**(9) p. 2472-2479 (2000)

20. E. Dugan, A. Jacobs, Z. Su, L. Houssay, D. Ekdahl and S. Brygoo, “Development and field testing of a mobile backscatter x-ray lateral migration radiography land mine detection system,” Proceeding of SPIE, **4742** p. 120-131 (2002)

21. E. Dugan, A. Jacobs, S. Keshavmurthy and J. Wehlburg," Lateral migration radiography", *Research in Nondestructive Evaluation*, **10**(2) p. 75-108 (1998)

22. A. Jacobs, E. Dugan, S. Brygoo, D. Ekdahl, L. Houssay and Z. Su, “Lateral migration radiography: a new x-ray backscatter imaging technique”, Proceeding of SPIE, **4786** p. 1-16 (2002)

23. E. Dugan, A. Jacobs, L. Houssay and D. Ekdahl, “Detection of flaws and defects using lateral migration x-ray radiography”, Proceeding of SPIE, **5199** p. 47-61 (2004)

24. M. Gertsenshteyn, T. Jannson, and G. Savant, “Staring/focusing lobster-eye hard x-ray imaging for non-astronomical objects”, Proceeding of SPIE, **5922** p. 107-117 2005)

25. A.P. Hammersley, “The reconstruction of coded-mask data under conditions realistic to x-ray astronomy observations”, Ph.D. Dissertation, University of Birmingham (1986)

26. R. Accorsi and R. Lanza, “Near-field artifact reduction in planar coded aperture imaging”, *Applied Optics*, **40**(26) p. 4697-4705 (2001)

27. A.A. Faust, R.E. Rothschild, and W.A. Heindl, "Development of a coded aperture backscatter imager using the UC San Diego HEXIS detector", Proceeding of SPIE , **5089** p. 95-106 (2003)

28. J.R.P Angel, "Lobster eyes as x-ray telescopes", *Astrophysical Journal,* **233** p. 364-373 (1979)

29. B.T. Addicott, "Characterization and optimization of radiography by selective detection backscatter x-ray imaging modality", M.S. Thesis, University of Florida (2006)

30. Glenn F. Knoll, "Radiation detection and measurement, 3rd edition", John Wiley & Sons, Inc. (1999)

31. B.L. Justus, P. Falkenstein, A.L. Huston, M.C. Plazas, H. Ning, and R.W. Miller "Gated fiber-optic-coupled detector for in vivo real-time radiation dosimetry" *Applied Optics,* **43**(8) p. 1663-1668 (2004)

32. E. Dugan, A. Jacobs, D Ekdahl, C. Meng, N. Sabri, D. Shedlock, "Research into the feasibility of utilizing various miniature diodes and x-ray detectors for x-ray backscatter", NASA Final Report, Award Number NNL05AF19P, (2006)

33. A. Saoudi, C.M. Pepin and R. Lecomte, "Study of light collection in multi-crystal detectors", *IEEE Transactions on Nuclear Science*, **47**(4) p. 1215-1219 (2000)

34. D. Shedlock, B. Addicott, E. T. Dugan, and A. M. Jacobs, "Optimization of a rsd x-ray backscatter system for detecting defects in the space shuttle external tank thermal foam insulation", Proceeding of SPIE, **5923** p. 205-216 (2005)

35. X-5 Monte Carlo Team, "MCNP - A general monte carlo, n-particle transport code, version 5", LA-UR-03-1987, Los Alamos National Laboratory (2003)

36. M.J. Berger, J.H. Hubbell, S.M. Seltzer, J. Chang, J.S. Coursey, R. Sukumar, and D.S. Zucker, "XCOM: Photon Cross Section Database (version 1.3) http://physics.nist.gov/xcom", National Institute of Standards and Technology (2007)

BIOGRAPHICAL SKETCH

Daniel Shedlock was born and raised in the small city of Wilkes-Barre, Pennsylvania. He completed a Bachelor of Science in Nuclear Engineering from Penn State University in 1997 and worked as a nuclear engineering consultant performing reactor decommissioning and radioactive waste management for WMG, Inc., before returning to Penn State University to complete a Master of Science in 2003 in the area of radiation shielding and transport theory. After the Columbia space shuttle accident in 2003 he began working on his Ph.D. in Nuclear and Radiological Engineering at the University of Florida in the area of Compton backscatter imaging (CBI). He helped to develop several of the CBI devices based on a new imaging technique called radiography by selective detection (RSD). The RSD scanning systems are still being used for inspection of the spray-on-foam-insulation on the external tank of the space shuttle to reduce the risk of another Columbia accident. In spring of 2007 he was part of the research team that invented a new CBI imaging technique, shadow aperture backscatter radiography (SABR). SABR allows single-exposure backscatter radiographs to be taken with any film-like radiation detector without any significant image processing. He started his own company Advanced Nuclear Services, LLC in 2006 to support the maintenance and research of the RSD scanning systems. In June of 2007 he joined NucSafe, Inc. as a senior scientist and business element manager, to quickly expedite the commercialization of the RSD scanning systems in the areas of non-destructive evaluation.